Molecular origins of genome instability following a single chromosome mis-segregation event

Giuseppina De Feudis[1,#], Lorenza Garribba[1,#], Valentino Martis[1], Martina Galli[2], Marie Dumont[3], Yonatan Eliezer[4], René Wardenaar[5], Marica Rosaria Ippolito[1], Divya R Iyer[6], Andréa E Tijhuis[5], Diana CJ Spierings[5], Michael Schubert[5], Nick Rhind[6], Floris Foijer[5], Uri Ben-David[4], Daniele Fachinetti[3], Ylli Doksani[2] and Stefano Santaguida[1,7,8,*]

1. Department of Experimental Oncology at IEO, European Institute of Oncology IRCCS, Via Adamello 16, 20139 Milan, Italy

2. IFOM ETS, the AIRC Institute of Molecular Oncology, via Adamello 16, 20139, Milan, Italy

3. Institut Curie, PSL Research University, CNRS, UMR144, Paris, France

4. Department of Human Molecular Genetics and Biochemistry, Faculty of Medicine, Tel Aviv University, Tel Aviv, Israel

5. European Research Institute for the Biology of Ageing, University of Groningen, University Medical Center Groningen, 9713 AV, Groningen, the Netherlands

6. Department of Biochemistry and Molecular Biotechnology, University of Massachusetts Chan Medical School, 364 Plantation Street, Worcester, MA 01605, USA

7. Department of Oncology and Hemato-Oncology, University of Milan, Via Santa Sofia 9/1, 20122 Milan, Italy

8. Lead Contact

#These authors contributed equally

*Correspondence: stefano.santaguida@ieo.it (SS)

Keywords: aneuploidy, cancer, genome instability, MiDAS, asymmetric DNA damage segregation, senescence, mitotic errors, chromosomal instability

Abstract

Genome instability is a hallmark of cancer. The most common form of genome instability is chromosomal instability (CIN), a condition in which cells mis-segregate their chromosomes during cell division. CIN leads to aneuploidy, a state of karyotype imbalance, often found in tumors. Although the causal relationship between CIN and aneuploidy is well established, evidence is limited for a direct involvement of aneuploidy in promoting CIN. Here, we show that aneuploid cells experience DNA replication stress in their first S-phase and precipitate in a state of continuous CIN, eventually accumulating complex karyotypes. Mechanistically, we find that aneuploid cells fire dormant replication origins through a Dbf4-dependent kinase (DDK)-driven mechanism and complete replication of genomic loci through mitotic DNA synthesis (MiDAS). By following the fate of aneuploid cells, we also show that, when they divide, DNA damage can be distributed asymmetrically between daughter cells, and this may partially explain why some aneuploid cells are able to continue proliferating and others stop dividing. We further found that cycling aneuploid cells display lower karyotype complexity compared to arrested ones and increased expression of gene signatures associated to DNA repair. Interestingly, by stratifying aneuploid human cancer cells by their doubling times, we found the same DNA repair signatures to be upregulated in highly-proliferative cancer cells, which might enable them to keep proliferating despite the disadvantage conferred by aneuploidy-induced genome instability. In summary, our study reveals the origins of genome instability following induction of aneuploidy and indicates the aneuploid state of cancer cells as a point mutation-independent source of genome instability, providing an explanation for the high occurrence of aneuploidy in tumors.

Introduction

Chromosomal instability (CIN), a condition of continuous chromosome mis-segregation, is a pervasive feature of tumors [1–4]. CIN confers enhanced evolutionary capabilities on cancer cells by increasing intratumor heterogeneity and by enabling chemoresistance [5–8]. CIN leads invariably to aneuploidy, a state of karyotype imbalances, found in more than 90% of solid tumors and about 65% of blood cancers [9]. The presence of aneuploid karyotypes leads to several detrimental defects, including proteotoxic stress [10–12], metabolic alterations [13] and induction of DNA damage [10,14–18]. Importantly, the presence of aneuploid karyotypes strongly correlates with poor patient prognosis [3]. This might be due to the fact that specific aneuploid karyotypes could confer a proliferative advantage, thus fueling tumorigenesis [7,8] and promoting survival under sub-optimal conditions [5,6]. Such an advantage could be explained by the possibility that aneuploidy induces CIN (and, more broadly, genome instability), which might enable a continuous sculpting of the genome, eventually

leading to cumulative haploinsufficiency and triplosensitivity [19,20] of genes crucial for sustained proliferation. In agreement with this idea, studies in yeast have demonstrated that gain of a single chromosome leads to defective DNA damage repair [15]. Further, aneuploid strains often divide in presence of unrepaired DNA, which triggers chromosomal translocations [21]. Similar observations were made in higher eukaryotes [22]. For example, a comparison between trisomic and diploid human cells has revealed that aneuploid cells are characterized by increased frequency of lagging chromosomes in anaphase [23,24]. Thus, this evidence points at aneuploidy as an instigator of genome instability [20]. It is plausible that this instability is due to the strong impact of karyotype abnormalities on gene expression and protein homeostasis. In fact, aneuploid cells were found to display imbalances in factors critical for DNA replication (such as MCM2-7), DNA repair and mitosis [17], processes that are all fundamental for the maintenance of genome integrity. In line with this possibility, our previous studies have revealed that aneuploid cells exhibit an increased S-phase duration, display reduced DNA replication fork rate and increased fork stalling [17,18]. Due to the intrinsic genomic instability and other stresses typically associated with aneuploidy, cells with abnormal karyotypes often exhibit delayed cell cycle progression. In some cases, they even lose their proliferative capacity and stop dividing [1,18,25], resulting in their reduced sensitivity to chemotherapies [26–28].

Given the high prevalence of unbalanced karyotypes in tumors and its impact on the proliferation of cancer cells [5–8], elucidating the contribution of aneuploidy to genome instability, deciphering the molecular mechanisms by which it occurs and deconvolving its cellular consequences remain of paramount importance in cancer biology.

Here, by inducing controlled chromosome mis-segregation in otherwise pseudo-diploid human cells, we set out to identify the origins of genome instability in aneuploid cells and to understand whether protective mechanisms operate to preserve genome integrity. Our data indicate that in the first S phase following chromosome mis-segregation, aneuploid cells fire dormant replication origins through a DDK-dependent mechanism and complete replication of genomic loci through mitotic DNA synthesis (MiDAS). Importantly, those pathways, acting both in interphase and mitosis, are crucial for aneuploid cells to protect them against further genome instability. We also show that the DNA damage associated with aneuploidy can be distributed asymmetrically between daughter cells during cell division and this, at least partially, can explain why some cells (*i.e.* those who have inherited most of the damage) stop dividing. By establishing a novel method for the separation of arrested and cycling aneuploid cells, we found that cycling aneuploid cells exhibit increased expression of DNA repair genes. Interestingly, the same transcriptional signature was upregulated in cancer cells characterized by high proliferative capacity. We speculate that elevated expression of DNA damage repair genes in highly proliferative cancers is able to help them counteracting the burden associated

with genome instability, allowing them to benefit from a continuous reshuffling of the karyotype, which is crucial to sustain enhanced proliferation [5,6]. Finally, we speculate that interfering with those pathways, including DDK-mediated origin firing and MiDAS, is crucial for limiting DNA damage and might provide novel therapeutic interventions in cancer therapy. An example of this is given by ongoing clinical trials involving agents inhibiting DDK-mediated origin firing (*e.g.*, ClinicalTrials.gov Identifier: NCT03096054 and NCT05028218), and our work might help in the stratification of patients who could benefit from those treatments based on their proliferative capacity.

Results

Identification of mechanisms responsible for tolerance to aneuploidy-induced replication stress

Aneuploidy is associated with increasing genome instability [20], affecting the fidelity of both genome replication and segregation. To dissect the mechanisms through which aneuploid cells seek to limit this instability and thus keep proliferating, we quantified the direct effects of aneuploidy on genome integrity. For this, we analyzed chromosome aberrations immediately after the induction of mitotic errors (1st mitosis) and after one cell cycle later (2nd mitosis). To this aim, we synchronized untransformed and genomically-stable, pseudo-diploid hTERT RPE-1 cells at the G1/S border and, after release into the cell cycle, pulsed them with DMSO (vehicle control) or reversine, an Mps1 inhibitor widely-used to generate aneuploid cells as a consequence of chromosome segregation errors [29]. Cells were then either harvested for karyotype analysis of the 1st mitosis or, after reversine wash-out, allowed to continue in the cell cycle, and then harvested for the same purpose in the 2nd mitosis (Fig. 1a). By doing so, analysis of 1st mitosis provided a measurement of the degree of chromosome aberrations directly caused by aneuploidy induction, whereas quantification of 2nd mitosis allowed for the estimation of genome alteration as a consequence of harboring aneuploid karyotypes. By using multi-color FISH (mFISH), we found abnormal events – including gains, losses and translocations – in both the 1st and 2nd mitoses (Fig. 1b,c and Extended Data Fig. 1a,b). Importantly, the percentage of cells harboring more than 10 abnormal events more than doubled from the 1st to the 2nd mitosis (Fig. 1b,c), indicating that the aneuploid state *per se* negatively impacts genome stability. To decipher how aneuploidy affects genome integrity, we examined at high resolution the 1st S phase of newly-generated aneuploid cells. For this, we used three complementary approaches: 1) ultra-structural visualization of replication forks through electron microscopy (EM), 2) single-cell analysis of replication stress and DNA damage markers by immunofluorescence and 3) assessment of replication dynamics by DNA combing (Fig. 1d). These efforts led to three key observations. First, EM analysis of replication intermediates revealed an increase in reversed replication forks in aneuploid cells, compared to pseudo-diploid counterparts (Fig. 1e,f). Accumulation of these intermediates is

associated with an increased frequency of replication fork stalling [30] and is consistent with previous observations of ongoing replication stress in aneuploid cells [18]. Further, aneuploid cells displayed increased levels of DNA replication stress and DNA damage markers such as FANCD2 (mean foci in control: 15,2 ± 1,9; aneuploid: 47,7 ± 4,6), RPA (mean foci in control: 10,6 ± 1,8; aneuploid 16,3 ± 2) and pChk1 (mean foci in control: 23 ± 1,8; aneuploid 33,3 ± 3,1) (Fig. 1g-l). Among them, the number of FANCD2 foci per S phase cell was found to be even higher in aneuploid cells than in cells treated with the DNA replication inhibitor aphidicolin, used as a positive control (FANCD2 mean foci in aphidicolin-treated cells: 40,7 ± 3; RPA mean foci 49 ± 3,9; pChk1 mean foci 44,1 ± 2,6) (Fig. 1h). Finally, we found that fork density and origin firing rate in aneuploid cells were higher than euploid counterparts (Fig. 1m-o), suggesting that dormant replication origins were fired in the 1st S phase following chromosome mis-segregation events. In our previous study we reported that aneuploid cells have reduced fork rate and a higher number of stalled forks as compared to euploid cells (Santaguida et al., 2017). Cells activate dormant origins in response to reduced fork rate and stalled forks to ensure that the genome gets fully replicated in time. Hence, we estimated origin firing rate and fork density, calculated as the total number of forks per Mb of DNA [31]. The total origin firing rate was 2-fold higher in aneuploid cells compared to euploid cells ($p=1,5x10^{-34}$). Consistent with the origin firing data, fork density was also 1,7-fold higher in aneuploid cells ($p=7,46x10^{-13}$). Analog-specific estimations for both the parameters also showed similar trends. Our data is also consistent with increased origin firing observed in aneuploid human pluripotent stem cells [32]. Overall our data shows that aneuploid cells struggle to complete replication and therefore activate backup mechanisms such as dormant origin firing to ensure genome duplication and tolerance of replication stress.

Altogether, these data provide crucial insights into the effects of aneuploidy on genome integrity. We find that 1) cells harboring aneuploid karyotypes tend to accumulate increasing levels of chromosome abnormalities. Importantly, 2) those defects might be the consequence of DNA replication stress, and 3) are correlated with a higher incidence of replication fork reversal and increased DNA damage markers. Finally, 4) at the same time, aneuploid cells also show an increased usage of dormant origins, which we speculate it might act as a mechanism to tolerate aneuploidy-induced replication stress.

Aneuploid cells rely on DDK to cope with replication stress

Dormant origin firing is a well-known rescue mechanism that protects cells during replication stress [33]. To test whether aneuploid cells would also rely on this salvage mechanism, we inhibited the activity of DDK, a key player in origin firing [34–37]. For this, aneuploid cells or pseudo-diploid counterparts (generated as in Fig. 1a) were arrested in late G1 (after the 1st mitosis) and then released in the presence or absence of the DDK inhibitor XL413 [38] (Fig. 2a). After 6 hours, cells were pulsed

with the thymidine analogue ethynyl deoxy-uridine (EdU) for 30 minutes to label S phase cells and then fixed and stained for FANCD2, RPA and pChk1. We find that inhibition of DDK led to significantly increased levels of FANCD2 (mean foci in control: 40,9 ± 2,9; control + DDKi: 52,6 ± 2,9; aneuploid 72,2 ± 3,5; aneuploid + DDKi: 84,5 ± 4,9), RPA (mean foci in control: 56,3 ± 3,7; control + DDKi: 36,2 ± 2,9; aneuploid 83,5 ± 5,8; aneuploid + DDKi: 103,9 ± 6,4) and pChk1 (mean foci in control: 44,1 ± 2,6; control + DDKi: 44,9 ± 2,8; aneuploid 62,9 ± 4,2; aneuploid + DDKi: 74,7 ± 4,2) in aneuploid cells, indicating that replication stress is exacerbated when interfering with dormant origin firing through DDK inhibition (Fig. 2b-g). These results prompted us to test whether DDK activity, and its involvement in dormant origin firing, would also be critical for aneuploid cell proliferation. Interestingly, we found that aneuploid cells were more sensitive to DDK inhibition compared to pseudo-diploid counterparts (Fig. 2h,i), indicating that they rely more than euploid cells on the function of DDK to survive. Altogether, our data show that DDK-mediated origin firing represents a protective mechanism that acts in S phase of aneuploid cells to limit replication stress. Importantly, inhibition of this mechanism exacerbates replication stress in aneuploid cells and reduces their viability.

Aneuploid cells undergo mitotic DNA synthesis to limit the consequences of replication stress on genome stability

DNA replication stress - defined as any slowing or stalling of replication fork progression and/or DNA synthesis [39] - impacts mitotic fidelity [40–42]. Thus, we thought to study how the events occurring in the 1st S phase of aneuploid cells affect the following cell division. To this aim, we performed live-cell imaging experiments with hTERT RPE-1 cells stably expressing PCNA-GFP and H2b-RFP. This allowed to monitor S phase length through the measurement of time elapsed between appearance and disappearance of PCNA foci (a well-known feature of this DNA clamping factor, [43]) and mitotic timing and quality by tracking chromosomes through H2b. Cells were synchronized with thymidine, then pulsed with reversine while they were transiting through the 1st mitosis. Cells were then washed-out and imaged every 10 minutes for 72 hours in order to evaluate the duration of the first S phase after chromosome mis-segregation and the quality of the 2nd mitosis (Fig. 3a,b). First, we found that aneuploid cells displayed a longer S phase compared to euploid controls (mean S phase length in control: 540,1 ± 17,82; aneuploid: 662,5 ± 29,89. Extended Data Fig. 1c), in agreement with the fact that they experience ongoing DNA replication stress and in line with previous reports [17,18]. Next, we decided to correlate S phase length to the quality of the 2nd mitosis. Thus, we classified mitotic figures in “normal mitoses”, for those not displaying defects, and “abnormal mitoses”, for those showing mitotic errors, including chromatin bridges, lagging chromosomes or micronuclei in the following

G1. Interestingly, we found a positive correlation between S phase length and frequency of abnormal mitoses (mean S phase length in control: 603,3 ± 55,4; aneuploid: 728,7 ± 46,2) (Fig. 3c). Further, aneuploid cells that displayed mitotic errors spent more time in mitosis (Fig. 3d), which we could fully attribute to spindle-assembly checkpoint activation, since SAC inhibition rescued this delay (Extended Data Fig. 1d).

Based on the evidence that aneuploid cells suffer from replication stress in the 1st S phase following chromosome mis-segregation events, we wanted to investigate whether they would attempt to finish DNA replication in the subsequent mitosis, as previously discovered in cancer cells as a consequence of S phase stress [44]. In order to evaluate mitotic DNA synthesis (MiDAS) pathway activation, aneuploid cells generated as in Fig. 1a were arrested at the G2/M boundary with the CDK1 inhibitor RO3306 and released in the presence of EdU and Colcemid to monitor sites of active DNA synthesis in prometaphase cells. We observed that the number of EdU foci per spread was significantly higher in aneuploid cells in comparison to the control (mean EdU foci in control: 0,1 ± 0,04; aneuploid: 0,9 ± 0,1; Fig. 3e,f). The DNA replication inhibitor aphidicolin was added in S phase as replication stress inducer (mean EdU foci: 2,6 ± 0,3) [45]. Next, to test the efficacy of MiDAS in fixing unfinished DNA replication, we inhibited the pathway and evaluated the consequences on genome stability in the following G1 (Fig. 3g). To this aim, we first tested if MiDAS could be inhibited by adding a high dose of aphidicolin in mitosis similarly as observed in cancer cells [44,46,47]. Our results showed that indeed this was the case, since the number of EdU foci per prometaphase cell was significantly reduced upon addition of aphidicolin in mitosis (mean EdU foci in control: 0,2 ± 0,1; control + MiDASi: 0,1 ± 0,03; aneuploid: 1,3 ± 0,2; aneuploid + MiDASi: 0,5 ± 0,1; Fig. 3H and I). As readouts of genome instability, we analyzed 53BP1 bodies and micronuclei in the G1 phase after the 2nd mitosis in which MiDAS had occurred. We found that both 53BP1 bodies per cell and the frequency of G1 cells with micronuclei were significantly increased in aneuploid cells in which MiDAS was inhibited in comparison with those in which MiDAS occurred properly (Fig. 3j-l). This correlation was also observed in aphidicolin-treated cells (mean EdU foci: 4,5 ± 0,6; + MiDASi: 0,7 ± 0,3), in agreement with previous studies [44]. Altogether, our data demonstrate that MiDAS acts as a safeguard mechanism in the 2nd mitosis to prevent genome instability from further increasing.

Dormant origin firing and MiDAS protect aneuploid cells from further increase in genome instability

The results obtained from the characterization of the first S phase after chromosome mis-segregation and the subsequent mitosis revealed two protective mechanisms operating in aneuploid cells with the role of limiting genome instability. To test if the combined action of these two pathways indeed serves

to protect aneuploid cells, we simultaneously inhibited DDK in S phase and MiDAS in the subsequent M phase and evaluated DNA damage and chromosomal aberrations in the following G1 phase (Fig. 4a). As DNA damage markers, we used FANCD2, a reliable replication stress/DNA damage marker in aneuploid cells (Fig. 1h), and γH2AX, an early marker of DNA double-stranded breaks [48]. To specifically look at G1 cells, we used cytochalasin B to block cytokinesis and analyze daughter cells (Fenech and Morley 1985). We observed that the number of both FANCD2 and γH2AX foci was significantly higher in aneuploid cells in which DDK and MiDAS were inhibited compared to aneuploid cells in which only either DDK or MiDAS was hindered (Fig. 4b-d). Interestingly, inhibition of those pathways led to an increase in FANCD2 and γH2AX foci also in euploid cells, highlighting that their proper functioning is crucial for maintaining genome integrity. Then, to assess the frequency of chromosomal aberrations upon DDK and MiDAS inhibition, G1 cells were treated with the PP1/PP2A phosphatase inhibitor calyculin A to induce premature DNA condensation [50] and obtain metaphase-like spreads. By mFISH analysis, we were able to observe an almost 2-fold increase in the percentage of cells with translocations between aneuploid cells in which DDK and MiDAS were or were not inhibited (mean percentage of cells with at least 1 translocation in aneuploid cells: 33,4; in aneuploid cells + DDKi + MiDASi: 63,2) (Fig. 4e-g). Taken together, these data indicate that the presence of both pathways protects aneuploid cells from further increasing their genome instability.

Interestingly, while scoring DNA damage in G1 cells we noticed that distribution of FANCD2 or γH2AX foci in aneuploid cells was not always symmetric between daughter cells. Thus, we decided to specifically look at the pattern of DNA damage inheritance in the aneuploid sample and the euploid control, along with aphidicolin-treated cells where it has been recently shown that DNA damage can be distributed asymmetrically between daughters [51]. Our data indicated that FANCD2 and γH2AX foci were asymmetrically distributed in about 20% and 10% of aneuploid daughter cells, respectively (Fig. 4h-j). These data suggested that non-random distribution of DNA damage between aneuploid daughter cells could underlie the difference in proliferation observed among aneuploid cells [18,25].

A novel method to separate arrested and cycling aneuploid cells

The asymmetric inheritance of DNA damage and cell fate determinants have been hypothesized to underlie stem cell self-renewal [52,53]. Thus, based on asymmetric portioning of DNA damage markers in aneuploid cells (Fig. 4h-j), we reasoned that, like stem cells, they might segregate DNA damage asymmetrically, partially explaining why some aneuploid cells can keep cycling while others get arrested and enter senescence [18,25]. To test this hypothesis, we first needed to confirm that a proportion of aneuploid cells indeed gets arrested in the cell cycle and becomes senescent over time. Hence, we

let aneuploid cells progress for about 3 cell cycles before harvesting them for β-galactosidase staining, a widely used marker of senescence [54]. As a positive control, we used cells treated with doxorubicin for 7 days, as DNA damage is an established senescence-inducer [55]. Our results indicated that, as expected [18], there was a sub-population of senescent cells in the aneuploid sample (Fig. 5a). In order to characterize, in detail, the aneuploid cells that were still able to cycle and those that underwent senescence, we decided to establish a novel method for their isolation and separation. For this, we reasoned that the main (and, at the same time, potentially exploitable) difference between aneuploid cycling and arrested cells is that the latter are senescent. Thus, we developed a FACS-sorting based assay employing the fluorescent substrate of the β-galactosidase enzyme (which is highly active in senescent cells) 9H-(1,3-dichloro-9,9-dimethylacridin-2-one-7-yl) β-d-galactopyranoside (DDAOG) [56]. We then exposed aneuploid cells to DDAOG and separated cells that were able to metabolize it (*i.e.*, senescent cells) from those that could not metabolize it (*i.e.*, cycling cells) (Fig. 5b,c; Extended Data Fig. 2a). First, we confirmed that sorted cells were indeed either arrested or cycling by β-galactosidase staining and found the former to be highly reactive to senescence-associated β-galactosidase staining (Fig. 5d). Further, we used hTERT FUCCI RPE-1 cells [57] to obtain the cell cycle profile of the two sorted aneuploid cell populations, together with the aneuploid sample before sorting and the euploid control (Extended Data Fig. 2b). Our data confirmed that aneuploid cells positive for DDAOG were indeed arrested, since the vast majority of them (86 ± 14,1%) were stuck in G1, as expected for senescent cells. On the other hand, negative ones were able to proliferate (Extended Data Fig. 2c and Fig. 5e,f) and the percentage of G1 cells were 24% (± 8,5%) (Extended Data Fig. 2c and Fig. 5e,f). Collectively, these data indicate that our method allows for the successful separation and recovery of arrested and cycling aneuploid cells that could be used for further analysis and characterization of the two populations.

Cell cycle arrest in aneuploid cells is due to both DNA damage and karyotype complexity

To validate our hypothesis that asymmetric inheritance of DNA damage would contribute to cell cycle arrest in aneuploid cells, we evaluated DNA damage in cycling and arrested aneuploid cells, together with aneuploid cells before sorting and the euploid control. Our data indicate that aneuploid arrested cells display increased levels of FANCD2 and γH2AX foci compared to aneuploid cycling cells (mean FANCD2 foci in aneuploid arrested: 71,8 ± 3,9; in aneuploid cycling: 46,9 ± 2,2; mean γH2AX foci in aneuploid arrested: 6,4 ± 1,1; in aneuploid cycling 2,4 ± 0,5) (Fig. 5g-i). Further, we also analyzed the karyotype of cycling and arrested aneuploid cells by single-cell whole genome sequencing (scWGS) and observed an increased frequency of cells with at least 3 aneuploid

chromosomes in arrested aneuploid cells (Fig. 5j,k). Altogether, these data show that both DNA damage and severe karyotype imbalances contribute to cell cycle arrest in aneuploid cells.

Cycling aneuploid cells display increased expression of DNA repair genes

In line with reduced DNA damage and karyotype abnormalities in the aneuploid cells that retained their proliferation capacity, we found that the frequency of mitotic errors (such as anaphase bridges and micronuclei) in aneuploid cycling cells was comparable to that of the controls for at least 3 generations by live-cell imaging (Fig. 6a-c). This result suggests that the karyotype of these cells is likely to remain stable over time, which is indicative of low levels of genome instability in aneuploid cycling cells. This also indicates that aneuploidy does not invariably leads to CIN and it suggests that specific chromosome assortments are more prone than others to be genomically unstable, reflecting imbalances of specific genes crucial for genome replication and segregation. Having established a tool to separate the two sub-populations of aneuploid cells, we turned our attention to the identification of features distinguishing aneuploid cycling cells from those that arrested. To address this question, we decided to analyze their transcriptional signatures via RNAseq. This analysis revealed that the two samples are indeed quite different (Fig. 6d). In particular, aneuploid arrested cells displayed overexpression of p53 and inflammation-related genes, in agreement with previous findings [18]. Conversely, aneuploid cycling cells, as expected based on their retained ability to divide, exhibited increased expression of cell cycle genes compared to aneuploid arrested cells. Interestingly, we also noticed that DNA damage and repair genes were overexpressed in aneuploid cycling cells (Fig. 6d and Extended Data Table 1). To further highlight differences in gene expression between the two subpopulations of aneuploid cells, we generated a heatmap showing that the main DNA repair related gene categories are more expressed in cycling *vs* arrested aneuploid cells (Fig. 6e). In line with this, when exposed to ionizing radiation (IR), cycling aneuploid cells were able to repair DNA damage more efficiently than the arrested ones (Extended Fig. 3a and Fig. 6f,g). Indeed, we measured a faster decay kinetics of γH2AX and 53BP1 levels in the cycling population compared to the arrested one (Extended Fig. 3a and Fig. 6f,g). Non-sorted aneuploid cells were also included in the analysis, and they turned out to have a lower efficiency compared to the euploid controls in fixing IR-induced DNA damage (Extended Fig. 3). Importantly, the activation of DNA damage repair pathways in aneuploid cells is consistent with our recent findings in cancer [27] and untransformed cells [58]. We therefore hypothesized that higher expression of DNA damage repair genes would confer a growth advantage to the cells. To confirm this, we turned to the CCLE (Cancer Cell Line Encyclopedia) database [59,60] to analyze the association between doubling time and DNA damage repair gene expression in more than 400 human cancer cell lines. We divided the cell lines into top and bottom

quartiles based on their doubling times, and then compared their gene expression profiles. Cells with a low doubling time (<35 hours) exhibited increased expression of DNA repair related gene signatures in comparison to cells with a high doubling time (>65 hours) (Fig. 6i-j), suggesting that elevated expression of this gene category can confer a proliferative advantage to aneuploid cells and make them able to cycle despite the disadvantage conferred by the aneuploid status. Altogether, our data revealed the existence of protective mechanisms in aneuploid cells, namely DDK-mediated origin firing in S phase and MiDAS in the subsequent mitosis, which operate in order to limit their genome instability (Fig. 7). Also, cell cycle arrest in aneuploid cells is due to not only the degree of karyotype aberrations but also to the levels of DNA damage harbored by the cells. Importantly, an increased capacity to repair DNA damage confers a proliferative advantage not only to untransformed but also to cancer aneuploid cells (Fig. 7).

Discussion

Genome instability is an established hallmark of cancer [61]. Its most common form is chromosomal instability (CIN), which has been shown to promote tumorigenesis and confer proliferative advantages to cancer cells [5–8]. Because CIN refers to a condition of continuous chromosome missegregation, this indicates that genomic instability can directly cause aneuploidy. In this study, we demonstrated that aneuploidy can also instigate genome instability. By combining biochemical and live cell imaging experiments with single-molecule replication-mapping technologies and single-cell multi-omics analysis, we found that the acquisition of unbalanced karyotypes can directly contribute to genome instability, which in turn yields a diverse array of karyotypic landscapes. This effect feeds a self-sustaining loop, in which aneuploidy leads to CIN, thus generating more aneuploid daughter cells able to propagate genome diversity through continuous errors during genome replication and segregation.

Previous reports have shown that aneuploid cells can experience replication stress [17,18]. Here, we show that dormant origin firing operates during the first S phase following chromosome mis-segregation and acts as a protective mechanism to cope with replication stress. The fact that DDK inhibition impacts on aneuploid cell viability reveals the importance of this pathway in the context of karyotype imbalances. Although we identified DDK-mediated dormant origin firing as a protective mechanism operating in the 1st S phase of aneuploid cells, it is still unclear what exactly triggers it, *i.e.* what are the actual sources of replication stress in cells with abnormal karyotypes. Many possible sources of DNA replication stress have been described so far, which include difficulties in the template DNA (*e.g.*, repetitive sequences and/or secondary structures), collisions between the replication fork and the transcriptional machinery, nucleotide pool imbalances and scarcity of

368 replication factors to perform DNA synthesis [39]. Among them, insufficient amount of replication
369 factors seems to be the most likely cause of replication stress in aneuploid cells, based on the fact that
370 decreased levels of MCM2-7 proteins were reported in RPE-1 and HCT116 stable aneuploid clones
371 with defined trisomies [17]. Also, a recent work has revealed that tetraploid cells encounter replication
372 stress as a result of insufficiency of DNA replication factors [62], a mechanism that could also apply to
373 aneuploid cells. Because in our system we observe dormant origin firing, we speculate that the
374 limiting DNA replication factors are those downstream of origin firing, such as PCNA, RFC and
375 DNA polymerases [63]. Future studies will be aimed at exploring this possibility, with the goal of
376 elucidating the contributions of those factors in DNA replication of aneuploid cells. This line of study
377 might also open novel therapeutic interventions through selective targeting of aneuploid cancer cells
378 by targeting those limiting DNA replication factors.
379 Along this line, another important implication of our finding that DDK and MiDAS play a central
380 role in helping cells coping with aneuploidy is that these mechanisms could well be targetable
381 vulnerabilities of aneuploid cancers. Although it might be challenging to selectively target MiDAS -
382 its key players SLX4-MUS81, RAD52 and POLD3 [44,46] are also involved in other processes beyond
383 MiDAS, such as homologous recombination (HR) repair and canonical S phase DNA replication –
384 things could be different for DDK. In particular, the DDK inhibitor TAK-931 was recently tested in
385 a phase 2 clinical trial for the treatment of advanced solid tumors [64]. Based on our study, we speculate
386 that this drug (and similar ones) could be combined with inhibitors of DNA repair, such as the
387 products of genes playing a role in HR repair, since they were the most differentially regulated in our
388 analysis (Extended Table 1). Thus, the combined inhibition of DDK and HR repair factors could
389 potentially be very effective to treat aneuploid cancers. This approach would have the great advantage
390 of being highly selective against cancer aneuploid cells, lowering the side-effects of the DNA repair-
391 based cancer therapies and the frequent chemoresistance associated with them [65].
392 In summary, by providing a detailed characterization of the role of aneuploid karyotypes in the
393 acquisition of aggressive cancer-like features, we demonstrate that aneuploidy provides a point
394 mutation-independent source of genome instability. Although this might offer a source of karyotypic
395 variations capable of enabling proliferative capacity of cancer cells, it also leads to extensive DNA
396 damage. Thus, we speculate that aneuploidy-induced genome instability might be a double-edged
397 sword for cancer cells. On one hand, it is crucial for providing genome plasticity, on the other it might
398 be extremely deleterious because of continuous DNA damage and replication stress. We propose that
399 cancer cells solve this issue by limiting DNA damage - through upregulation of DNA repair genes -
400 to a level compatible with cell proliferation. At the same time, this allows them to keep some degree
401 of genomic instability and thus to continuously sample diverse karyotypic landscapes. Our

observation shed new light on the bidirectional association between aneuploidy and genomic instability and propose new approaches for the selective eradication of aneuploid tumors.

Methods

Cell culture conditions

hTERT RPE-1 cells, including those expressing H2b-RFP and PCNA-GFP or H2b-GFP or LCK-GFP (all generated in house) and the hTERT Fluorescent Ubiquitination-based Cell Cycle Indicator (FUCCI) RPE-1 (kind gift of Professor Simona Polo, IFOM, Milan, Italy), were all tested free of mycoplasma contamination using Myco Alert (Lonza) according to manufacturer's instructions. All the cells were maintained in a humified environment at 37 degrees with 5% CO_2 and cultured in Dulbecco's modified Eagle's medium (DMEM) supplemented with 10% fetal bovine serum and 1% penicillin/streptamycin.

Cell synchronization and treatments

To harvest metaphase cells for mFISH analysis, hTERT RPE-1 cells were pulsed with the Mps1 inhibitor reversine (500nM, Cayman Chemical) or the vehicle control (dimethyl sulfoxide, DMSO) for 24 hours and then harvested for karyotype analysis either immediately after the pulse ('1st mitosis') or 24 hours later ('2nd mitosis'). In both cases, colcemid (100ng/ml, Merck Millipore) was added 2 hours before harvesting the cells in order to block cells in prometaphase. To perform ultra-structural analysis of replication intermediates and analyze replication dynamics, cells were treated as above and analyzed immediately after the 24-hour reversine/DMSO pulse.

To analyze DNA replication stress markers in S phase, hTERT RPE-1 cells were plated onto fibronectin (5µg/ml, Sigma-Aldrich) coated coverslips at approximately 30% confluence and synchronized at the G1/S boundary with thymidine (5mM, Merck Millipore) for 24 hours. After 3 washes in 1X PBS, cells were pulsed for 18 hours with reversine or vehicle control (DMSO) and released in the presence of mimosine (0,5mM, Merck Millipore) for 18 hours. After 3 washes in 1X PBS, cells were incubated for 6 hours in the presence or absence of aphidicolin (400nM, Merck Millipore) or the DDK inhibitor XL413 (10µM, Aurogene) prior to fixation for immunofluorescence. The thymidine analog ethynyl deoxy-uridine (EdU) was added at a final concentration of 10µM during the last 30 minutes to label S phase cells.

To assess S phase length and quality of the subsequent mitosis by time-lapse microscopy, after plating onto a fibronectin-coated glass 12wellplate, hTERT RPE-1 cells were blocked in G1/S with thymidine for 24 hours, then washed out, pulsed with reversine/DMSO for 18 hours and filmed for 72 hours.

For MiDAS detection, hTERT RPE-1 cells were treated as above and, after reversine/DMSO washout, released in RO3306 (7,5µM, Merck Millipore) for 12 hours to arrest them in late G2 phase. Then, after 3 washes in 1X PBS, cells were released in mitosis in the presence of EdU 20µM and colcemid for 2 hours to harvest prometaphase cells for MiDAS detection. Aphidicolin 400nM was added to a subpopulation of cells pulsed with DMSO just after DMSO washout in order to induce DNA replication stress (positive control). To investigate the consequences of MiDAS inhibition in G1 cells, cells were plated and treated as above. After RO3306 washout, cells were released in EdU 20µM in the presence or absence of aphidicolin (2µM, Merck Millipore) for 40 minutes (for prometaphase cells) or 3 hours (for G1 cells) prior to fixation of immunofluorescence.

In order to harvest daughter pseudo-G1 cells, after thymidine and reversine pulses, hTERT RPE-1 LCK-GFP cells were released in the presence or absence of XL413 10µM and arrested in late G2 phase with RO3306 7,5µM. After drug washout, cells were incubated in the presence or absence of aphidicolin 2µM for 3 hours together with cytochalasin B (3µg/ml, Merck Millipore) to block cytokinesis prior to fixation for immunofluorescence.

To obtain metaphase-like spreads from G1 cells, calyculin A (50ng/ml, Sigma-Aldrich) was added for 45 minutes to G1 cells treated as above to induce premature chromosome condensation, prior to harvest for mFISH analysis.

To evaluate β-galactosidase positivity in aneuploid cells, after reversine washout, hTERT RPE-1 cells were allowed to progress for about 60 hours before fixation. The same protocol was used to generate aneuploid cells for sorting, including hTERT FUCCI RPE-1 and hTERT RPE-1 H2b-GFP cells. After sorting, some cells were replated and fixed 16 hours later to perform β-galactosidase staining, while some other were replated for live cell imaging experiments or directly harvested as frozen pellets for RNA extraction. As a positive control for senescence, cells continuously treated with doxorubicin (200nM, Merck Millipore) for 7 days were used.

Multicolor fluorescence in situ hybridization (mFISH)

After the treatments described above, hTERT RPE-1 cells blocked in prometaphase or G1 cells in which premature condensation was induced were trypsinized and centrifuged to obtain cell pellets. Cell pellets were resuspended in KCl 75mM and incubated for 10 min in a 37 degrees waterbath. After centrifugation, cells were fixed in freshly-prepared Carnoy solution (methanol-acetic acid in a 3:1 ratio) while vortexing and then incubated for 30 minutes at room temperature (RT). After a wash in freshly-prepared Carnoy solution, minimum volume of fixative was left to resuspend the pellet and cells were dropped onto glass slides. mFISH staining was performed following manufacturer's instructions (MetaSystems). The Metafer imaging platform (MetaSystems) and the Isis software

(MetaSystems, version 5.5) were used for automated acquisition of the chromosome spread and mFISH image analysis.

Ultra-structural analysis of replication intermediates

For EM analysis, hTERT RPE-1 cells were pulsed for 24 hours with reversine or vehicle control (DMSO) and then harvested. Immediately after, cells were psoralen-crosslinked *in vivo* to stabilize replication intermediates as described in [66]. The cell suspension was first incubated with 30 µg/ml 4, 5′, 8-trimethylpsoralen (2mg/ml, Sigma) for 5 min in the dark and then exposed to 365 nm UV light for 8 min in a UV Stratalinker 1800, (Stratagene), with 365 nm UV bulbs (model UVL-56, UVP) at 2–3 cm from the light source. The incubation and irradiation steps were repeated three more times (4 cycles total). Genomic DNA (gDNA) was extracted with phenol-chloroform as described in [66]. 50 µg of gDNA were digested with KpnI and passed through a QIAGEN Genomic-tip 20/G column (QIAGEN) to enrich for replication intermediates, as described by Zellweger and Lopes [67]. EM spreads and imaging was performed as described in [68].

Immunofluorescence analysis and EdU detection

At the end of the treatments described above, hTERT RPE-1 or hTERT RPE-1 LCK-GFP cells were washed once in 1X PBS and then fixed in 4% paraformaldehyde (PFA) for 15 minutes at RT. After 3 washes in 1X PBS, cells were blocked in 3% bovine serum albumin (BSA) + 0.5% Triton-X in 1X PBS for 30 minutes and incubated with the following primary antibodies diluted in the same buffer for 90 minutes at RT: anti-FANCD2 (Novus Biologicals) 1:400, anti-RPA (Abcam) 1:200, anti-pChk1 (Cell Signaling Technology) 1:200, anti-53BP1 (Abcam) 1:1000, anti-γH2AX (Millipore) 1:400. After 3 washes in 1X PBS, cells were incubated with secondary antibodies (ThermoFisher Scientific) diluted 1:400 in 3% BSA + 0.5% Triton-X in 1X PBS for 45 minutes at RT in the dark. Coverslips were then mounted on glass slides using Vectashield Antifade Mounting Medium with DAPI (Vectorlabs).

Where indicated, immunofluorescence was combined with EdU detection. Briefly, after the blocking, EdU detection was performed using the Click-iT EdU Cell Proliferation kit for Imaging (ThermoFisher Scientific) following the manufacturer's instructions. After the washes, incubation of the cells in primary antibodies and the subsequent steps of immunofluorescence were performed as indicated above.

DNA fiber analysis

Cells were labeled sequentially with IdU (green [G]) and CldU (red [R]) and were harvested and

processed as described in [18]. Data was collected from 2 independent experiments. A total of 47 and 54 Mb of DNA and 33 and 38 Mb of DNA was collected from the control and the aneuploid cells, respectively. Data analysis was performed as described in detail in [31]. Please note that the order of labeling is reversed (CldU → IdU) in the experiments described in [31], therefore, the interpretation of patterns is also reversed as compared to this article. Briefly, origin firing rate is the total number of origins that fired during the first and the second analog in each fiber divided by the total length of the un-replicated DNA in that fiber and the total length of the analog labeling pulses (120 minutes). Origins that fire during the first analog will appear as Red-Green-Red [RGR] and origins that fire during the second analog will appear as Red [R] events. However, origins that fire during the first analog will appear as RGR only if both the forks progress into the second analog. The origins will appear as RG or GR if either of the fork stalls or as G if both the forks stall. Thus, the total number of origins in each fiber was estimated by accounting for the probability of forks stalling.

Fork density is the total number of forks in each fiber divided by the total length of the un-replicated DNA of that fiber. Origins and termination events account for 2 forks each and unidirectional fork events account for 1 fork each. However, some of the unidirectional forks could be an origin whose left or rightward fork is stalled. Thus, the total number of forks on each fiber was estimated by accounting for the probability of forks stalling. Please see [31] for calculation of fork stall rate and how the probability of fork stalling was used to estimate the final origin firing rate and fork density for each fiber.

Cell proliferation assay

After thymidine synchronization and reversine/DMSO pulse as above, hTERT RPE-1 cells were trypsinized, counted and plated into a 96wellplate in the presence of XL413 10μM or the vehicle control (DMSO). Drugs were re-added fresh every 48-72 hours during the 120 hour -treatment. Then, cell viability was assessed by using the CellTiter-Glo Luminescent cell viability assay (Promega) following manufacturer's instructions.

Live cell imaging

To monitor S phase length and M phase duration and quality, cells were treated as above. After reversine/DMSO washout, fresh medium without phenol red was added to the cells. Cells were imaged every 10 minutes for 72 hours under a 20x objective with an inverted Nikon Eclipse Ti microscope equipped with incubator for live cell imaging. The same microscope and acquisition settings were used to film aneuploid cycling cells after sorting for 72 hours to assess their genome stability.

538

539 **MiDAS detection**

540 To detect MiDAS on metaphase spreads, after incubation in EdU and colcemid as above, cells were
541 treated similarly to those for mFISH analysis. After cell dropping onto glass slides and complete
542 evaporation of the Carnoy solution, slides washed in 1X PBS in agitation. EdU detection was
543 performed with the Click-iT EdU Cell Proliferation kit for Imaging (ThermoFisher Scientific)
544 according to manufacturer's instructions with some minor modifications as described in [69]. Slides
545 were then mounted using Vectashield Antifade Mounting Medium with DAPI.
546 To detect MiDAS on prometaphase cells, at the end of the treatments described above, cells were
547 fixed in 4% PFA for 15 minutes at RT, then washed 3 times in 1X PBS. EdU detection was performed
548 as above [69] and coverslips were then mounted on glass slides using the same mounting medium as
549 above.

550

551 **Distribution of DNA damage in pseudo-G1 cells**

552 First, the number of FANCD2 and γH2AX foci per daughter cell was counted. Based on the average
553 number of foci per cell, cells with less than 6 or 4 foci (for FANCD2 or γH2AX, respectively) were
554 excluded from the analysis. Then, the total number of foci between the two daughters (*e.g.* 13+10)
555 was calculated and divided by 2 to obtain the number of foci predicted to be inherited by each
556 daughter cell in case of symmetric distribution of DNA damage (*e.g.* 23 divided by 2 is equal to 11,5).
557 Subtraction or addition of this number to the total number of foci in the daughters was used to set a
558 threshold for asymmetric distribution of DNA damage, *e.g.* 23-11,5= 11,5, which is the lowest
559 threshold; 23+11,5= 34,5, which is the highest threshold; if a daughter cell has less than 11,5 or more
560 than 34,5 foci the distribution of DNA damage is considered as non-random (non-random
561 distribution, NDD).

562

563 **β-galactosidase staining**

564 DMSO- and reversine-pulsed cells allowed to progress for about 72 hours after DMSO/reversine
565 washout, together with sorted cycling and arrested aneuploid cells, were plated into a 6 well plate at
566 $1x10^6$ cells/well and allowed to attach overnight. Then, cells were stained using the Senescence β-
567 Galactosidase Staining Kit (Cell Signaling Technology) following manufacturer's instructions.

568

569 **Sorting of aneuploid cells**

570 Cells were plated into 150 mm plates (900.000 cells/plate) and treated as above. After
571 reversine/DMSO washout, cells were allowed to divide for about 60 hours. Then, they were incubated

with the fluorescent substrate of the β-galactosidase enzyme DDAO-Galactoside (DDAOG) 10mM for 90 minutes. At the end of the incubation, cells were harvested for FACS sorting and acquired using a FACSAria Fusion flow cytometer (BD). Cells were gated for singlets and alive cells and then FSC-A, SSC-A and Alexa-647 intensity were used to distinguish cycling from arrested cells, *i.e.* cycling cells were gated using the same Alexa-647 Mean Fluorescence Intensity of the control sample without DDAOG, while arrested cells were gated imposing 0,1% on Alexa-647 signal to the control sample without DDAOG. FlowJo was used to perform data analysis and generate the plots in Figure 5 and Extended Data Fig. 2.

Cell cycle profile analysis through the FUCCI system

hTERT FUCCI RPE-1 cells were used to generate euploid, aneuploid, cycling aneuploid and arrested aneuploid cells as described above. After the sorting, cells were plated in a 12wellplate, allowed to attach overnight and then filmed using an inverted Nikon Eclipse Ti microscope with a 40x objective equipped with incubator for live cell imaging. Brightfield, green (GFP) and red (mCherry) channels were used to acquire the movie. Images were taken every 30 minutes for 24 hours. Cell cycle stage was determined based on nuclear color: red nuclei were scored as G1 phase, while yellow and green nuclei were scored as S/G2 phase; lastly, M phase was characterized by uncolored nuclei of two dividing cells [57].

Sample processing for RNAseq

Aneuploid cycling and arrested cells post sorting were centrifuged and cell pellets were obtained. RNA was extracted from them using a RNeasy kit (QIAGEN) and its quality was assessed with a Bioanalyzer 2100 (Agilent). Then, for each sample, total RNA was depleted of ribosomal RNA and the RNAseq libraries were prepared with the Illumina TruSeq Stranded Total RNA kit following the manufacturer's protocol. Briefly, after the fragmentation of RNA using divalent cations at elevated temperature, cDNA was synthesized, end-repaired and 3'-end-adenylated. Following adapter ligation, libraries were amplified by PCR. Amplified libraries were checked on a Bioanalyzer 2100 (Agilent) and quantified with picogreen reagent. Libraries with distinct TruSeq adapter UDIndexes were sequenced for 50 bases in the paired-end mode with 35 million reads in coverage on a Novaseq 6000 sequencer.

Data analysis for RNAseq

RNA reads were aligned to the GRCh38 primary assembly with Ensembl 104 [70] gene annotations using. STAR 2.7.9a [71]. Gene counts were quantified with subread 2.0.2 [72]. Differentially expressed

606 genes were determined using DESeq2 1.30.0 [73] with a Wald test, regressing out for the batch factor.
607 Subsequently, genes were filtered based on significance (P-value ≤0.05 and PADJ ≤0.25; for the
608 aneuploid vs. control analysis results were filtered only based on p-value). Pre-ranked gene set
609 enrichment analysis (PreRanked GSEA) was performed to identify enriched pathways [74]. Single cell
610 gene set enrichment analysis (ssGSEA) was performed using GenePatterns [74,75], to compare the
611 expression of specific DNA damage-related signatures across samples. Z-scores were calculated for
612 each gene signature across and plotted as a heatmap. Plots were generated using the Python's
613 'seaborn' library (Van Rossum and Drake, 2009).
614
615 **Kinetics of DNA repair upon exposure to IR**
616 After cell sorting (as described above), aneuploid cycling and arrested cells, together with non-sorted
617 aneuploid cells and euploid controls, were plated on coverslips and incubated overnight. The day
618 after, cells were γ-irradiated (1.25Gy) and fixed for immunofluorescence as indicated above at
619 different timepoints. In order to exclude S phase cells, cells were pulsed with EdU 10μM for 30
620 minutes before fixation. Non-irradiated cells were fixed together with the first timepoint. i.e. 0h post
621 irradiation.
622
623 **Association of DDR gene expression with doubling time**
624 CCLE (Cancer cell line encyclopedia) gene expression data were obtained from DepMap
625 (https://depmap.org/portal/) 22Q1 release [60] and cell line doubling times were obtained from
626 Tsherniak et al. 2017. Cell lines were divided to quartiles according to their doubling time, while
627 ssGSEA scores were generated using the GenePattern platform (https://www.genepattern.org/) [74,75]
628 and compared between the top and bottom quartiles. Statistical analysis (two-tailed Student' t-test)
629 and plotting were performed using GraphPad PRISM v9.3.1.
630
631 **Sample processing for single-cell whole genome sequencing (scWGS)**
632 Cell pellets were resuspended in cell lysis buffer (100mM Tris-HCl pH 7.4, 154mM NaCl, 1mM
633 $CaCl_2$, 500μM $MgCl_2$, 0,2% BSA, 0,1% NP-40, 10μg/ml Hoechst 33358, 2μg/ml propidium iodide
634 in ultra-pure water) and incubated on ice in the dark for 15 minutes to ensure complete lysis. Resulting
635 single nuclei of G1 phase (as determined by Hoechst and PI staining) were sorted into single wells of
636 96 wellplates on a MoFlo Astrios cell sorter (Beckman Coulter) and sorted at -80C until firther
637 processing. Automated library preparation was performed (Bravo Automated Liquid Handling
638 Platform, Agilent Technologies) as previously described [76]. Resulting single-cell libraries were
639 pooled for subsequent sequencing.

640

641 **Data analysis for scWGS**

642 Sequencing was performed using a NextSeq 500 machine (Illumina; up to 77 cycles – single end or
643 up to 68 and 9 cycles – paired end; excluding sample-specific barcodes). Reads were afterwards
644 aligned to the human reference genome (GRCh38/hg38) using Bowtie2 (version 2.2.4 or 2.3.4.1;
645 Langmead and Salzberg 2012). Duplicate reads were marked with BamUtil (version 1.0.3; [77]) or
646 Samtools markdup (version 1.9; [78]. The aligned read data (bam files) were analyzed with a copy
647 number calling algorithm called AneuFinder (https://github.com/ataudt/aneufinder; [79]). Following
648 GC correction and blacklisting of artefact-prone regions (extreme low or high coverage in control
649 samples), libraries were analyzed using the dnacopy and edivisive copy number calling algorithms
650 with variable width bins (average bin size = 1 Mb; step size = 500 kb). Results were afterwards
651 curated by requiring a minimum concordance of 95% between the results of the two algorithms.
652 Libraries with on average less than 10 reads per bin (~ 30,000 reads for a diploid genome) were
653 discarded. A chromosome was classified as aneuploid when at least 95 % of the bins showed a
654 deviation from euploid (deviation from 2-somy). Chromosomes 10 and 12 were excluded for the
655 calculation of whole-genome scores.

656

657 **Quantification and statistical analysis**

658 Statistical analyses were performed using GraphPad Prism software. Statistical significance in each
659 case was calculated using Student's t-test, Chi-squared test or Fisher's exact test. Error bars represent
660 SEMs or SDs. All experiments were performed in at least three biological replicates, with some
661 exceptions (see Figure legends).

662

663 ## References

664 1. Santaguida S, Amon A. Short- and long-term effects of chromosome mis-segregation and
665 aneuploidy. *Nat Rev Mol Cell Biol*. 2015;16(8):473-485. doi:10.1038/nrm4025
666 2. Levine MS, Holland AJ. The impact of mitotic errors on cell proliferation and tumorigenesis.
667 *Genes Dev*. 2018;32(9-10):620-638. doi:10.1101/gad.314351.118
668 3. Ben-David U, Amon A. Context is everything: aneuploidy in cancer. *Nat Rev Genet*.
669 2020;21(1):44-62. doi:10.1038/s41576-019-0171-x
670 4. Al-rawi DH, Bakhoum SF. Chromosomal instability as a source of genomic plasticity. *Curr*
671 *Opin Genet Dev*. 2022;74:101913. doi:10.1016/j.gde.2022.101913
672 5. Ippolito MR, Martis V, Martin S, et al. Gene copy-number changes and chromosomal
673 instability induced by aneuploidy confer resistance to chemotherapy. *Dev Cell*.

2021;56(17):2440-2454.e6. doi:10.1016/j.devcel.2021.07.006

6. Lukow DA, Sausville EL, Suri P, et al. Chromosomal instability accelerates the evolution of resistance to anti-cancer therapies. *Dev Cell*. 2021;56(17):2427-2439.e4. doi:10.1016/j.devcel.2021.07.009

7. Shoshani O, Bakker B, De Haan L, et al. Transient genomic instability drives tumorigenesis through accelerated clonal evolution. *Genes Dev*. 2021;35(15-16):1093-1109. doi:10.1101/gad.348319.121

8. Trakala M, Aggarwal M, Sniffen C, et al. Clonal selection of stable aneuploidies in progenitor cells drives high-prevalence tumorigenesis. *Genes Dev*. 2021;35(15-16):1079-1092. doi:10.1101/gad.348341.121

9. Vasudevan A, Baruah PS, Smith JC, et al. Single-Chromosomal Gains Can Function as Metastasis Suppressors and Promoters in Colon Cancer. *Dev Cell*. 2020;52(4):413-428.e6. doi:10.1016/j.devcel.2020.01.034

10. Ohashi A, Ohori M, Iwai K, et al. Aneuploidy generates proteotoxic stress and DNA damage concurrently with p53-mediated post-mitotic apoptosis in SAC-impaired cells. *Nat Commun*. 2015;6. doi:10.1038/ncomms8668

11. Santaguida S, Vasile E, White E, Amon A. Aneuploidy-induced cellular stresses limit autophagic degradation. *Genes Dev*. 2015;29(19):2010-2021. doi:10.1101/gad.269118.115

12. Stingele S, Stoehr G, Peplowska K, Cox J, Mann M, Storchova Z. Global analysis of genome, transcriptome and proteome reveals the response to aneuploidy in human cells. *Mol Syst Biol*. 2012;8(608). doi:10.1038/msb.2012.40

13. Williams BR, Prabhu VR, Hunter KE, et al. and Spontaneous Immortalization. *October*. 2008;322(October):703-710.

14. Torres EM, Sokolsky T, Tucker CM, et al. Effects of aneuploidy on cellular physiology and cell division in haploid yeast. *Science (80-)*. 2007;317(5840):916-924. doi:10.1126/science.1142210

15. Sheltzer JM, Blank HM, Pfau SJ, et al. Aneuploidy drives genomic instability in yeast. *Science (80-)*. 2011;333(6045):1026-1030. doi:10.1126/science.1206412

16. Zhu J, Pavelka N, Bradford WD, Rancati G, Li R. Karyotypic determinants of chromosome instability in Aneuploid budding yeast. *PLoS Genet*. 2012;8(5). doi:10.1371/journal.pgen.1002719

17. Passerini V, Ozeri-Galai E, De Pagter MS, et al. The presence of extra chromosomes leads to genomic instability. *Nat Commun*. 2016;7. doi:10.1038/ncomms10754

18. Santaguida S, Richardson A, Iyer DR, et al. Chromosome Mis-segregation Generates Cell-

Cycle-Arrested Cells with Complex Karyotypes that Are Eliminated by the Immune System. *Dev Cell*. 2017;41(6):638-651.e5. doi:10.1016/j.devcel.2017.05.022

19. Davoli T, Xu AW, Mengwasser KE, et al. XCumulative haploinsufficiency and triplosensitivity drive aneuploidy patterns and shape the cancer genome. *Cell*. 2013;155(4):948. doi:10.1016/j.cell.2013.10.011

20. Garribba L, Santaguida S. The Dynamic Instability of the Aneuploid Genome. *Front Cell Dev Biol*. 2022;10. doi:10.3389/fcell.2022.838928

21. Blank HM, Sheltzer JM, Meehl CM, Amon A. Mitotic entry in the presence of DNA damage is a widespread property of aneuploidy in yeast. *Mol Biol Cell*. 2015;26(8):1440-1451. doi:10.1091/mbc.E14-10-1442

22. Burrell RA, McClelland SE, Endesfelder D, et al. Replication stress links structural and numerical cancer chromosomal instability. *Nature*. 2013;494(7438):492-496. doi:10.1038/nature11935

23. Nawata H, Kashino G, Tano K, et al. Dysregulation of gene expression in the artificial human trisomy cells of chromosome 8 associated with transformed cell phenotypes. *PLoS One*. 2011;6(9). doi:10.1371/journal.pone.0025319

24. Nicholson JM, Macedo JC, Mattingly AJ, et al. Chromosome mis-segregation and cytokinesis failure in trisomic human cells. *Elife*. 2015;4(MAY):1-23. doi:10.7554/eLife.05068

25. Wang RW, Viganò S, Ben-David U, Amon A, Santaguida S. Aneuploid senescent cells activate NF-κB to promote their immune clearance by NK cells. *EMBO Rep*. 2021;22(8):1-16. doi:10.15252/embr.202052032

26. Lee AJX, Endesfelder D, Rowan AJ, et al. Chromosomal instability confers intrinsic multidrug resistance. *Cancer Res*. 2011;71(5):1858-1870. doi:10.1158/0008-5472.CAN-10-3604

27. Cohen-Sharir Y, McFarland JM, Abdusamad M, et al. Aneuploidy renders cancer cells vulnerable to mitotic checkpoint inhibition. *Nature*. 2021;590(7846):486-491. doi:10.1038/s41586-020-03114-6

28. Replogle JM, Zhou W, Amaro AE, et al. Aneuploidy increases resistance to chemotherapeutics by antagonizing cell division. *Proc Natl Acad Sci U S A*. 2020;117(48):30566-30576. doi:10.1073/pnas.2009506117

29. Santaguida S, Tighe A, D'Alise AM, Taylor SS, Musacchio A. Dissecting the role of MPS1 in chromosome biorientation and the spindle checkpoint through the small molecule inhibitor reversine. *J Cell Biol*. 2010;190(1):73-87. doi:10.1083/jcb.201001036

30. Neelsen KJ, Lopes M. Replication fork reversal in eukaryotes: From dead end to dynamic response. *Nat Rev Mol Cell Biol*. 2015;16(4):207-220. doi:10.1038/nrm3935

31. Iyer DR, Rhind N. *Replication Fork Slowing and Stalling Are Distinct, Checkpoint-Independent Consequences of Replicating Damaged DNA*. Vol 13.; 2017. doi:10.1371/journal.pgen.1006958

32. Lamm N, Ben-David U, Golan-Lev T, Storchová Z, Benvenisty N, Kerem B. Genomic Instability in Human Pluripotent Stem Cells Arises from Replicative Stress and Chromosome Condensation Defects. *Cell Stem Cell*. 2016;18(2):253-261. doi:10.1016/j.stem.2015.11.003

33. Ge XQ, Jackson DA, Blow JJ. Dormant origins licensed by excess Mcm2-7 are required for human cells to survive replicative stress. *Genes Dev*. 2007;21(24):3331-3341. doi:10.1101/gad.457807

34. Jares P, Blow JJ. Xenopus Cdc7 function is dependent on licensing but not on XORC, XCdc6, or CDK activity and is required for XCdc45 loading. *Genes Dev*. 2000;14(12):1528-1540. doi:10.1101/gad.14.12.1528

35. Tanaka S, Umemori T, Hirai K, Muramatsu S, Kamimura Y, Araki H. CDK-dependent phosphorylation of Sld2 and Sld3 initiates DNA replication in budding yeast. *Nature*. 2007;445(7125):328-332. doi:10.1038/nature05465

36. Labib K. Howdo Cdc7 and cyclin-dependent kinases trigger the initiation of chromosome replication in eukaryotic cells? *Genes Dev*. 2010;24(12):1208-1219. doi:10.1101/gad.1933010

37. Heller RC, Kang S, Lam WM, Chen S, Chan CS, Bell SP. Eukaryotic origin-dependent DNA replication in vitro reveals sequential action of DDK and S-CDK kinases. *Cell*. 2011;146(1):80-91. doi:10.1016/j.cell.2011.06.012

38. Koltun ES, Tsuhako AL, Brown DS, et al. Discovery of XL413, a potent and selective CDC7 inhibitor. *Bioorganic Med Chem Lett*. 2012;22(11):3727-3731. doi:10.1016/j.bmcl.2012.04.024

39. Zeman MK, Cimprich KA. Causes and consequences of replication stress. *Nat Cell Biol*. 2014;16(1):2-9. doi:10.1038/ncb2897

40. Chan KL, Palmai-Pallag T, Ying S, Hickson ID. Replication stress induces sister-chromatid bridging at fragile site loci in mitosis. *Nat Cell Biol*. 2009;11(6):753-760. doi:10.1038/ncb1882

41. Mankouri HW, Huttner D, Hickson ID. How unfinished business from S-phase affects mitosis and beyond. *EMBO J*. 2013;32(20):2661-2671. doi:10.1038/emboj.2013.211

42. Wilhelm T, Olziersky AM, Harry D, et al. Mild replication stress causes chromosome mis-

776 segregation via premature centriole disengagement. *Nat Commun*. 2019;10(1):1-14.
777 doi:10.1038/s41467-019-11584-0
778 43. Ellison V, Stillman B. Biochemical characterization of DNA damage checkpoint complexes:
779 Clamp loader and clamp complexes with specificity for 5′ recessed DNA. *PLoS Biol*.
780 2003;1(2). doi:10.1371/journal.pbio.0000033
781 44. Minocherhomji S, Ying S, Bjerregaard VA, et al. Replication stress activates DNA repair
782 synthesis in mitosis. *Nature*. 2015;528(7581):286-290. doi:10.1038/nature16139
783 45. Baranovskiy AG, Babayeva ND, Suwa Y, Gu J, Pavlov YI, Tahirov TH. Structural basis for
784 inhibition of DNA replication by aphidicolin. *Nucleic Acids Res*. 2014;42(22):14013-14021.
785 doi:10.1093/nar/gku1209
786 46. Bhowmick R, Minocherhomji S, Hickson ID. RAD52 Facilitates Mitotic DNA Synthesis
787 Following Replication Stress. *Mol Cell*. 2016;64(6):1117-1126.
788 doi:10.1016/j.molcel.2016.10.037
789 47. Garribba L, Bjerregaard VA, Gonçalves Dinis MM, et al. Folate stress induces SLX1- And
790 RAD51-dependent mitotic DNA synthesis at the fragile X locus in human cells. *Proc Natl*
791 *Acad Sci U S A*. 2020;117(28):16527-16536. doi:10.1073/pnas.1921219117
792 48. Bonner WM, Redon CE, Dickey JS, et al. γH2AX and cancer. *Nat Rev Cancer*.
793 2008;8(12):957-967. doi:10.1038/nrc2523
794 49. Fenech M, Morley AA. Measurement of micronuclei in lymphocytes. *Mutat Res*. 147(1-
795 2):29-36. doi:10.1016/0165-1161(85)90015-9
796 50. Miura T, Blakely WF. Optimization of calyculin A-induced premature chromosome
797 condensation assay for chromosome aberration studies. *Cytom Part A*. 2011;79 A(12):1016-
798 1022. doi:10.1002/cyto.a.21154
799 51. Xing M, Zhang F, Liao H, et al. Replication Stress Induces ATR/CHK1-Dependent
800 Nonrandom Segregation of Damaged Chromosomes. *Mol Cell*. 2020;78(4):714-724.e5.
801 doi:10.1016/j.molcel.2020.04.005
802 52. Cairns J. Mutation selection and the natural history of cancer. *Nature*. 1975;255(5505):197-
803 200. doi:10.1038/255197a0
804 53. Rocheteau P, Gayraud-Morel B, Siegl-Cachedenier I, Blasco MA, Tajbakhsh S. A
805 subpopulation of adult skeletal muscle stem cells retains all template DNA strands after cell
806 division. *Cell*. 2012;148(1-2):112-125. doi:10.1016/j.cell.2011.11.049
807 54. Dimri GP, Lee X, Basile G, et al. A biomarker that identifies senescent human cells in
808 culture and in aging skin in vivo. *Proc Natl Acad Sci U S A*. 1995;92(20):9363-9367.
809 doi:10.1073/pnas.92.20.9363

55. Campisi J, D'Adda Di Fagagna F. Cellular senescence: When bad things happen to good cells. *Nat Rev Mol Cell Biol*. 2007;8(9):729-740. doi:10.1038/nrm2233

56. Macedo JC, Vaz S, Bakker B, et al. FoxM1 repression during human aging leads to mitotic decline and aneuploidy-driven full senescence. *Nat Commun*. 2018;9(1):1-17. doi:10.1038/s41467-018-05258-6

57. Sakaue-Sawano A, Kurokawa H, Morimura T, et al. Visualizing Spatiotemporal Dynamics of Multicellular Cell-Cycle Progression. *Cell*. 2008;132(3):487-498. doi:10.1016/j.cell.2007.12.033

58. Zerbib J, Ippolito MR, Reuveni E, et al. Aneuploid cells depend on the RAF/MEK/ERK pathway and on RNA degradation for overcoming DNA damage and transcriptional burden. *In_Submission*.

59. Tsherniak A, Vazquez F, Montgomery PG, et al. Defining a Cancer Dependency Map. *Cell*. 2017;170(3):564-576.e16. doi:10.1016/j.cell.2017.06.010

60. Ghandi M, Huang FW, Jané-Valbuena J, et al. Next-generation characterization of the Cancer Cell Line Encyclopedia. *Nature*. 2019;569(7757):503-508. doi:10.1038/s41586-019-1186-3

61. Hanahan D. Hallmarks of Cancer: New Dimensions. *Cancer Discov*. 2022;12(1):31-46. doi:10.1158/2159-8290.CD-21-1059

62. Gemble S, Wardenaar R, Keuper K, et al. Genetic instability from a single S phase after whole-genome duplication. *Nature*. 2022;604(7904):146-151. doi:10.1038/s41586-022-04578-4

63. Fragkos M, Ganier O, Coulombe P, Méchali M. DNA replication origin activation in space and time. *Nat Rev Mol Cell Biol*. 2015;16(6):360-374. doi:10.1038/nrm4002

64. Iwai K, Nambu T, Dairiki R, et al. Molecular mechanism and potential target indication of TAK-931, a novel CDC7-selective inhibitor. *Sci Adv*. 2019;5(5). doi:10.1126/sciadv.aav3660

65. Pilié PG, Tang C, Mills GB, Yap TA. State-of-the-art strategies for targeting the DNA damage response in cancer. *Nat Rev Clin Oncol*. 2019;16(2):81-104. doi:10.1038/s41571-018-0114-z

66. Mazzucco G, Huda A, Galli M, Zanella E, Doksani Y. Purification of mammalian telomeric DNA for single-molecule analysis. *Nat Protoc*. Published online 2022:1-27. doi:10.1038/s41596-022-00684-9

67. Kolstø AB. *Genome Instability*. Vol 106.; 1998. doi:10.1111/j.1600-0463.1998.tb05651.x

68. Mazzucco G, Huda A, Galli M, et al. Telomere damage induces internal loops that generate telomeric circles. *Nat Commun*. 2020;11(1). doi:10.1038/s41467-020-19139-4

69. Garribba L, Wu W, Özer Ö, Bhowmick R, Hickson ID, Liu Y. Inducing and Detecting Mitotic DNA Synthesis at Difficult-to-Replicate Loci. *Methods Enzymol*. 2018;601:45-58. doi:10.1016/bs.mie.2017.11.025

70. Yates AD, Achuthan P, Akanni W, et al. Ensembl 2020. *Nucleic Acids Res*. 2020;48(D1):D682-D688. doi:10.1093/nar/gkz966

71. Dobin A, Davis CA, Schlesinger F, et al. STAR: Ultrafast universal RNA-seq aligner. *Bioinformatics*. 2013;29(1):15-21. doi:10.1093/bioinformatics/bts635

72. Liao Y, Smyth GK, Shi W. FeatureCounts: An efficient general purpose program for assigning sequence reads to genomic features. *Bioinformatics*. 2014;30(7):923-930. doi:10.1093/bioinformatics/btt656

73. Love MI, Huber W, Anders S. Moderated estimation of fold change and dispersion for RNA-seq data with DESeq2. *Genome Biol*. 2014;15(12):1-21. doi:10.1186/s13059-014-0550-8

74. Subramanian A, Tamayo P, Mootha VK, et al. Gene set enrichment analysis: A knowledge-based approach for interpreting genome-wide expression profiles. *Proc Natl Acad Sci U S A*. 2005;102(43):15545-15550. doi:10.1073/pnas.0506580102

75. Reich M, Liefeld T, Gould J, Lerner J, Tamayo P, Mesirov JP. GenePattern 2.0. *Nat Genet*. 2006;38(5):500-501. doi:10.1038/ng0506-500

76. van den Bos H, Bakker B, Taudt A, et al. Quantification of Aneuploidy in Mammalian Systems. *Methods Mol Biol*. 2019;1896:159-190. doi:10.1007/978-1-4939-8931-7_15

77. Jun G, Wing MK, Abecasis GR, Kang HM. An efficient and scalable analysis framework for variant extraction and refinement from population-scale DNA sequence data. *Genome Res*. 2015;25(6):918-925. doi:10.1101/gr.176552.114

78. Danecek P, Bonfield JK, Liddle J, et al. Twelve years of SAMtools and BCFtools. *Gigascience*. 2021;10(2):1-4. doi:10.1093/gigascience/giab008

79. Bakker B, Taudt A, Belderbos ME, et al. Single-cell sequencing reveals karyotype heterogeneity in murine and human malignancies. *Genome Biol*. 2016;17(1):1-15. doi:10.1186/s13059-016-0971-7

80. Zhang CZ, Spektor A, Cornils H, et al. Chromothripsis from DNA damage in micronuclei. *Nature*. 2015;522(7555):179-184. doi:10.1038/nature14493

Acknowledgments

We are very grateful to all the members of the Santaguida group for fruitful discussions throughout the project. We thank Elsa Logarinho and members of M. Mapelli lab for constructive discussions. Work in the Santaguida lab is supported by grants from the Italian Association for Cancer Research

(MFAG 2018 - ID. 21665 project), Ricerca Finalizzata (GR-2018-12367077), Fondazione Cariplo, the Rita-Levi Montalcini program from MIUR and the Italian Ministry of Health with Ricerca Corrente and 5x1000 funds. L.G. is supported by a fellowship from Fondazione IEO-Monzino. Work in the Ben-David lab is supported by grants from the European Research Council (ERC grant #945674), Israel Cancer Research Foundation Gesher Award, Israel Science Foundation (ISF grant #1805/21), the DoD CDMRP Career Development Award (grant #CA191148), the Azrieli Faculty Fellowship and the EMBO Young Investigator Program.

Figure legends

Fig. 1: Aneuploid cells accumulate increasing genome instability and display higher levels of DNA replication stress markers in S phase. a, Experimental setup for the analysis of genome instability of cells obtained from the 1st and the 2nd mitosis. Karyotype aberrations were assessed by mFISH analysis. **b,c,** Representative mFISH images of karyotypes obtained from the 1st and the 2nd mitosis in aneuploid cells and relative quantification. T(10,X) and +12 were excluded from the analysis as they are clonal in hTERT RPE-1 cells. **d,** Schematic representation of the experimental approaches used for the study of the 1st S phase after induction of chromosome missegregation. A short EdU pulse was performed before cell harvest in order to label S phase cells to be analyzed by immunofluorescence. **e,f,** Representative images of normal and reversed replication forks analyzed by electron microscopy and quantification of the reversed ones in control and aneuploid cells. 108 and 95 forks were analyzed in the control and in the aneuploid sample, respectively. **g,h,** Representative images and quantification of FANCD2 foci per S phase cell in control and aneuploid cells. **i,j,** Representative images and quantification of RPA foci per S phase cell in control and aneuploid cells. **k,l,** Representative images and quantification of pChk1 foci per S phase cell in control and aneuploid cells. Cells treated with aphidicolin (RS, replication stress) were used as a positive control. **m,** Representative images of DNA fiber analysis in control and aneuploid cells. **n,o,** Quantification of (**n**) fork density per Mb and (**o**) origin firing rate per Mb in control and aneuploid cells. Ctrl, control (DMSO pulsed). Aneu, aneuploid cells (Mps1 inhibitor pulsed). RS, replication stress (aphidicolin treated cells). Scale bars, 5μm. LUT was inverted for FANCD2, RPA and pChk1 images. Data are means of at least three biological replicates, except for the EM (one replicate) and the DNA combing (two replicates) analyses. Error bars represent SEMs. ** denotes p<0,01; **** denotes p <0,001.

Fig. 2: DDK protects aneuploid cells from DNA damage accumulation and consequent cell death. a, Experimental workflow for the analysis of DNA replication stress markers in S phase cells

upon treatment with the DDK inhibitor XL-413. A short EdU pulse was performed before cell harvest in order to label S phase cells. **b,c,** Representative images and quantification of FANCD2 foci per S phase cell in control or aneuploid cells ± DDK inhibitor. **d,e,** Representative images and quantification of RPA foci per S phase cell in control or aneuploid cells ± DDK inhibitor. **f,g,** Representative images and quantification of pChk1 foci per S phase cell in control or aneuploid cells ± DDK inhibitor. **h,** Experimental workflow for the assessment of cell viability upon exposure to the DDK inhibitor. **i,** Quantification of live cells upon DDK inhibitor treatment in control and aneuploid cells. Ctrl, control (DMSO pulsed). Aneu, aneuploid cells (Mps1 inhibitor pulsed). DDKi, DDK inhibitor. Scale bars, 5µm. LUT was inverted for FANCD2, RPA and pChk1 images. Data are means of at least three biological replicates. Error bars represent SEMs. * denotes p<0,05; ** denotes p<0,01; *** denotes p< 0,005; **** denotes p<0,001.

Fig. 3: MiDAS protects aneuploid cells from a further increase in their genome instability. a, Experimental workflow for the analysis of the 1st S phase duration, 2nd M phase duration and quality by live-cell imaging in hTERT RPE-1 cells expressing H2b-RFP and PCNA-GFP. **b,** Representative images from the movies of mitosis duration and quality in control and aneuploid cells. **c,d,** Correlation between (**c**) S phase duration and quality of the subsequent mitosis and (**d**) mitotic timing and mitotic quality in control and aneuploid cells. **e,f**, Representative images and quantification of EdU incorporation on metaphase spreads in control and aneuploid cells. Cells treated with aphidicolin (RS, replication stress) were used as a positive control. **g,** Experimental workflow for the assessment of genome instability in the following G1 phase upon MiDAS inhibition. **h,i,** Representative images and quantification of EdU incorporation in prometaphase cells upon MiDAS inhibition. Cells treated with aphidicolin (RS, replication stress) were used as a positive control. **j,k,l,** Representative images (**j**) and quantification of 53BP1 body (**k**) and micronucleus (**l**) accumulation in G1 cells following inhibition of MiDAS. Ctrl, control (DMSO pulsed). Aneu, aneuploid cells (Mps1 inhibitor pulsed). RS, replication stress (aphidicolin treated cells). MiDASi, MiDAS inhibitor. Normal M, normal mitosis. Abnormal M, abnormal mitosis. Scale bars, 5 or 10 µm. Data are means of at least three biological replicates. Error bars represent SEMs. * denotes p<0,05; **denotes p<0,01; *** denotes p< 0,005; **** denotes p<0,001.

Fig. 4: DDK and MiDAS act as surveillance mechanisms to limit genome instability accumulation in aneuploid cells. a, Experimental workflow for the analysis of DNA damage and chromosome aberrations in G1 cells following DDK and MiDAS inhibition in the cell cycle after chromosome missegregation induction. **b,c,d,** Representative images (**b**) and quantification of

946 FANCD2 (**c**) and γH2AX (**d**) accumulation in cytokinesis-blocked pseudo-G1 cells expressing LCK-
947 GFP. **e**, Representative mFISH images of G1 cell-derived metaphase-like chromosomes from
948 aneuploid cells upon DDK and MiDAS inhibition. **f**, Zoomed image of the chromosome highlighted
949 in the dotted-line box in panel E (image on the right) from the aneuploid sample in which DDK and
950 MiDAS were inhibited showing a translocation between chromosome 19 and chromosome 18. **g**,
951 Quantification of the percentage of cells with more than 1 translocation in the two samples. **h,i,j**,
952 Representative images (**h**) and quantification of FANCD2 (**i**) and γH2AX (**j**) non-random distribution
953 between the daughter pseudo-G1 cells. Cells treated with aphidicolin (RS, replication stress) were
954 used as a positive control. Ctrl, control (DMSO pulsed). Aneu, aneuploid cells (Mps1 inhibitor
955 pulsed). RS, replication stress (aphidicolin treated cells). MiDASi, MiDAS inhibitor. NDD, non-
956 random distribution. Scale bars, 5 or 10 μm. Data are means of at least three biological replicates,
957 except for data in panels e-g that were obtained from two biological replicates. Error bars represent
958 SEMs. * denotes p<0,05; ** denotes p<0,01; *** denotes p< 0,005; **** denotes p<0,001.
959
960 **Fig. 5: Aneuploid cells that retained their proliferative capacity exhibit reduced levels of DNA**
961 **damage and genome instability. a**, Senescence-associated β-galactosidase staining in control and
962 aneuploid cells. Doxorubicin-treated cells were used as a positive control. **b**, Experimental workflow
963 for a new method to separate and recover both cycling and arrested aneuploid cells based on FACS-
964 sorting and the usage of a fluorescent substrate of the b-galactosidase enzyme. **c**, FACS profiles
965 showing the percentage of DDAOG-positive cells in aneuploid cells incubated or not with the
966 DDAOG substrate. **d**, Senescence-associated β-galactosidase staining in cycling and arrested
967 aneuploid cells obtained after sorting. **e**, Cell cycle profiles of control, aneuploid, aneuploid cycling
968 and aneuploid arrested FUCCI-cells analyzed by live-cell imaging. **f**, Quantification of percentage of
969 G1 cells in the four samples analyzed by live-cell imaging. **g,h,i,** Representative images (**g**) and
970 quantification of FANCD2 (**h**) and γH2AX (**i**) foci per cell in the different samples. Only EdU
971 negative cells were analyzed in order to exclude the contribution of S phase cells present in the non-
972 arrested cell samples. **j**, scWGS of cycling and arrested aneuploid cells. Single cells are represented
973 in rows and chromosomes plotted as columns. Copy-number states are indicated in colors (see legend
974 on the right). hTERT RPE-1 cells have clonal gains of 10q and chromosome 12 [80]. **k,** Quantification
975 of cells with at least 3 aneuploid chromosomes in the two samples. Gains of 10q and chromosome 12
976 were excluded from the analysis. Ctrl or Ct, control (DMSO pulsed). Aneu or An, aneuploid cells
977 (Mps1 inhibitor pulsed). Aneu cycling or An cy, aneuploid cycling cells. Aneu arrested or An ar,
978 aneuploid arrested cells. Scale bars, 5μm. Data are means of at least three biological replicates, except

for panel f (one replicate). Error bars represent SEMs, except for panel E (SDs). * denotes p<0,05; **** denotes p<0,001.

Fig. 6: Cycling aneuploid cells display decreased karyotype aberrations and upregulate DNA repair genes in comparison with arrested aneuploid cells. a, Experimental workflow for the assessment of genome instability levels by live-cell imaging in aneuploid cycling cells expressing H2b-GFP. **b**, Representative images of cell divisions in the different samples. **c**, Quantification of mitotic errors in 3 cell division rounds in control and aneuploid cycling cells. Cells treated with the Mps1 inhibitor just before starting the time-lapse were used as a positive control for mitotic errors. **d**, Volcano plot illustrating the differentially expressed pathways between cycling and arrested aneuploid cells. Specific gene sets are highlighted in color. **e,** Heat-map showing the z-scores of single-sample GSEA (ssGSEA) scores for DNA damage-related gene sets. **f,g,** Quantification of γH2AX foci (f) and 53BP1 bodies (g) in cycling and arrested aneuploid cells upon IR exposure. Only EdU negative cells were analyzed in order to exclude the contribution of S phase cells present in the non-arrested cell samples. **h,i,j,** Association between ssGSEA score for GOBP DNA repair (**h**) or GOBP DNA synthesis involved in DNA repair (**i**) or GOBP regulation of DNA repair (**j**) and proliferation capacity in top vs. bottom quartiles of cancer cell lines from [59]. Aneu cycling or An cy, aneuploid cycling cells. Aneu arrested or An ar, aneuploid arrested cells. M, mother division. D, daughter division. GD, grand-daughter division. Mps1i, Mps1 inhibitor. #1 and #2 refer to biological replicates. Not irrad., not irradiated. Data are means of at least two biological replicates. Error bars represent SEMs. Shaded error bands in panels f,g are shown above and below for arrested and cycling cells, respectively. **** denotes p<0,001; ns, not significant.

Fig. 7: Final model. A model for how aneuploidy induces genome instability and its consequences. See text for more details.

Extended Data Fig. 1: Impact of chromosome mis-segregation induction on karyotype changes, S and M phase. a, Representative images of the karyotype obtained from the 1st and the 2nd mitosis in control cells. **b**, Quantification of percentage of cells with chromosome gains, losses or translocations in the 1st or 2nd mitosis in control cells. **c**, Quantification of S phase duration by live-cell imaging in control and aneuploid cells. The graph refers to the experiment in Figure 3, panels A-D. **d**, Quantification of mitotic division timing upon SAC inhibition in control and aneuploid cells that underwent normal or abnormal mitosis. Ctrl, control (DMSO pulsed). Aneu, aneuploid cells

(Mps1 inhibitor pulsed). Mps1i, Mps1 inhibitor. Data are means of at least three biological replicates. Error bars represent SEMs. *** denotes p<0,005; **** denotes p<0,001.

Extended Data Fig. 2: Separation and characterization of aneuploid cycling and arrested cells. **a**, FACS profiles showing the percentage of DDAOG positive cells in DMSO and doxorubicin treated cells, used as a positive control. **b,** Illustration depicting the change in nuclear color in the FUCCI cells. **c**, Representative images showing the starting (0h) and end point (24h) of the time-lapse in the four different samples. Scale bar 20μm.

Extended Data Fig. 3: Kinetics of DNA damage repair in aneuploid cells and respective controls upon IR exposure. a,b, Representative images (**a**) and quantification (**b**) of γH2AX foci per cell. **c,d,** Representative images (**c**) and quantification (**d**) of 53BP1 bodies per cell. Only EdU negative cells were analyzed in order to exclude the contribution of S phase cells present in the non-arrested cell samples. Ctrl, control (DMSO pulsed). Aneu, aneuploid cells (Mps1 inhibitor pulsed). Aneu cycling, aneuploid cycling cells. Aneu arrested, aneuploid arrested cells. Not irrad., not irradiated. Data are means of two biological replicates. Shaded error bands in panels f,g are shown above and below for aneuploid cells and euploid controls, respectively.

Extended Data Table 1: List of genes differentially expressed in arrested vs. cycling aneuploid cells. Data were obtained by RNAseq (Fig. 6).

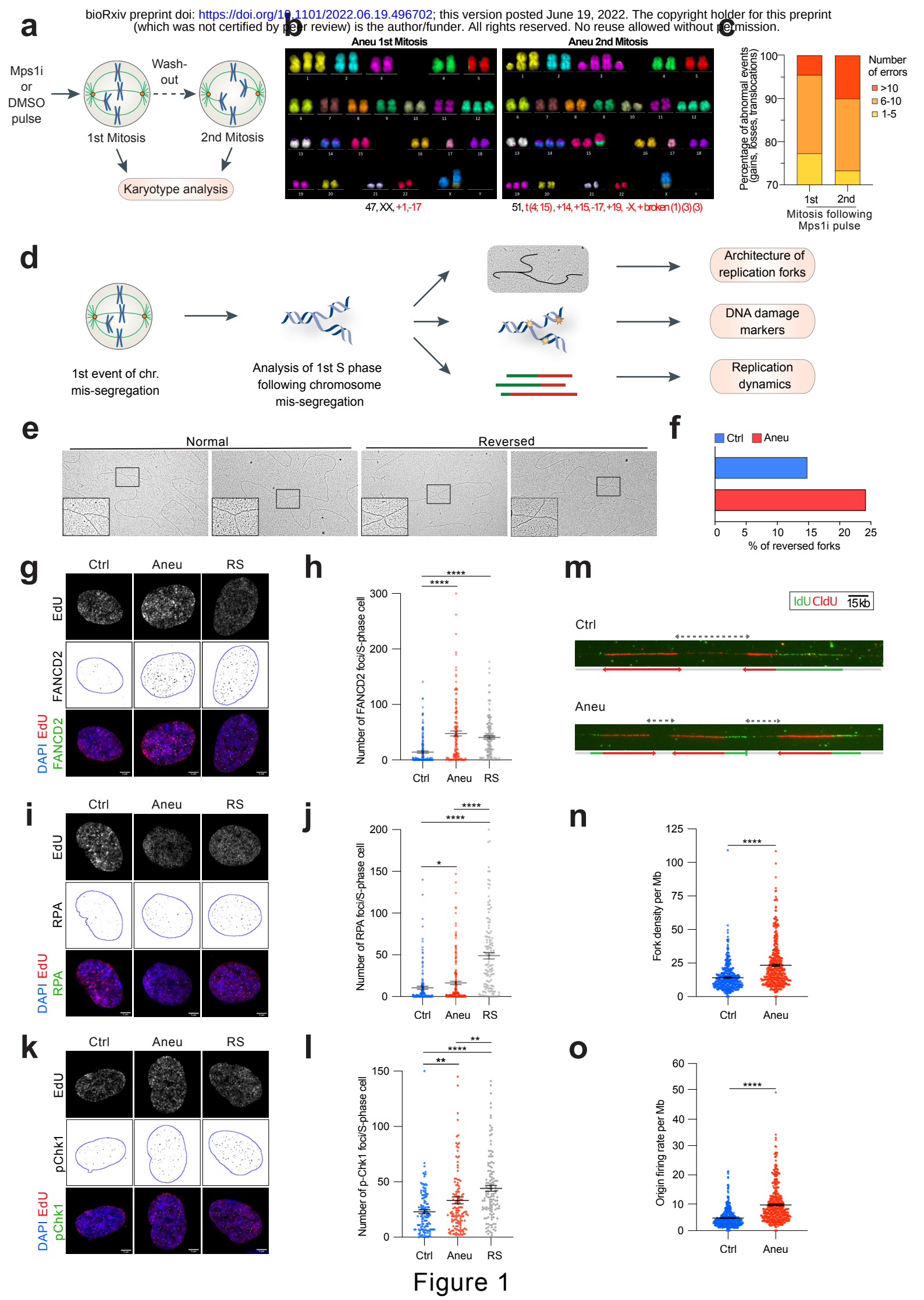

Figure 1

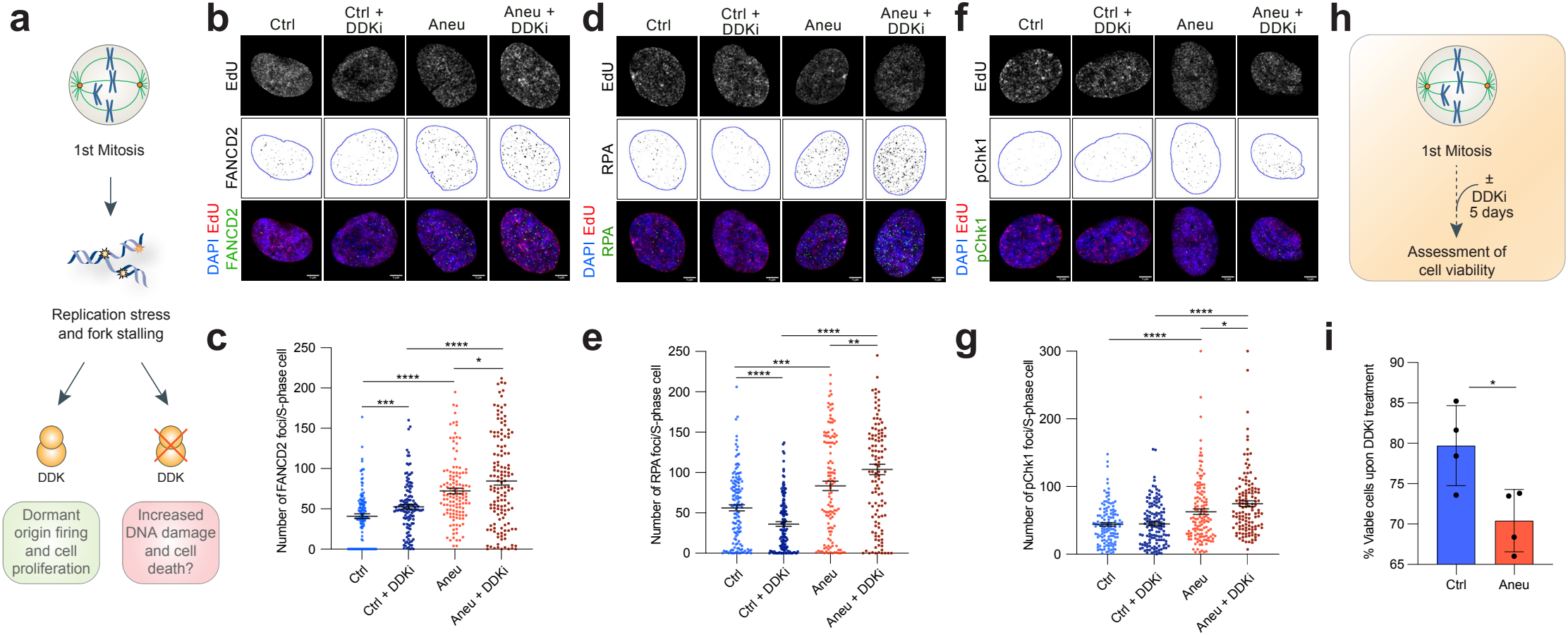
a
1st Mitosis
Replication stress and fork stalling
DDK
DDK
Dormant origin firing and cell proliferation
Increased DNA damage and cell death?
b
Ctrl
Ctrl + DDKi
Aneu
Aneu + DDKi
EdU
FANCD2
DAPI EdU FANCD2
c
Number of FANCD2 foci/S-phase cell
d
RPA
DAPI EdU RPA
e
Number of RPA foci/S-phase cell
f
pChk1
DAPI EdU pChk1
g
Number of pChk1 foci/S-phase cell
h
1st Mitosis
± DDKi 5 days
Assessment of cell viability
i
% Viable cells upon DDKi treatment

Figure 2

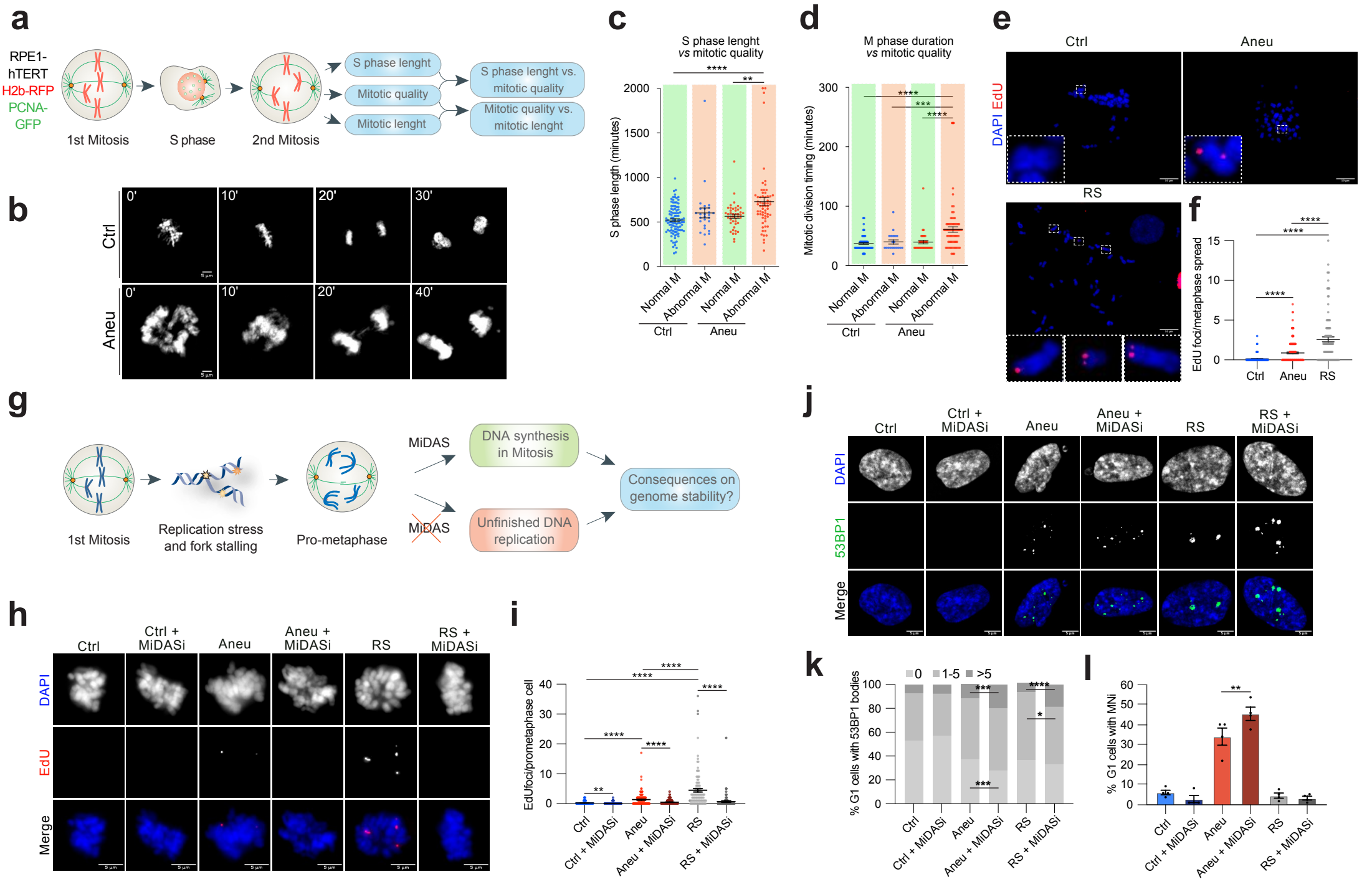
a
RPE1-hTERT H2b-RFP PCNA-GFP
1st Mitosis
S phase
2nd Mitosis
S phase lenght
Mitotic quality
Mitotic lenght
S phase lenght vs. mitotic quality
Mitotic quality vs. mitotic lenght
b
Ctrl
Aneu
0'
10'
20'
30'
40'
c
S phase lenght vs mitotic quality
S phase length (minutes)
Normal M
Abnormal M
Ctrl
Aneu
d
M phase duration vs mitotic quality
Mitotic division timing (minutes)
e
Ctrl
Aneu
RS
DAPI EdU
f
EdU foci/metaphase spread
g
1st Mitosis
Replication stress and fork stalling
Pro-metaphase
MiDAS
DNA synthesis in Mitosis
Unfinished DNA replication
Consequences on genome stability?
h
Ctrl
Ctrl + MiDASi
Aneu
Aneu + MiDASi
RS
RS + MiDASi
DAPI
EdU
Merge
i
EdUfoci/prometaphase cell
j
DAPI
53BP1
Merge
k
% G1 cells with 53BP1 bodies
0
1-5
>5
l
% G1 cells with MNi

Figure 3

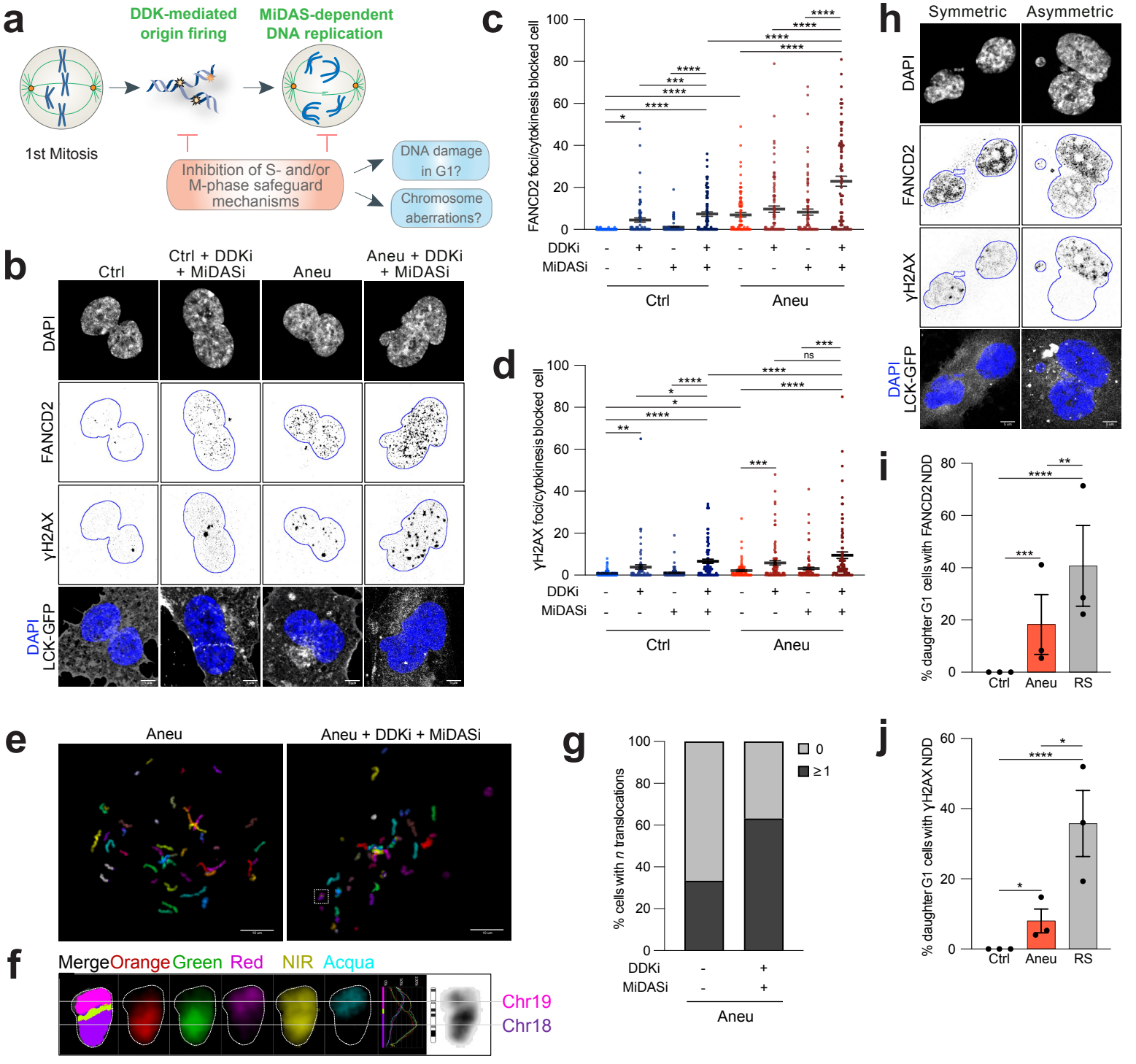

Figure 4

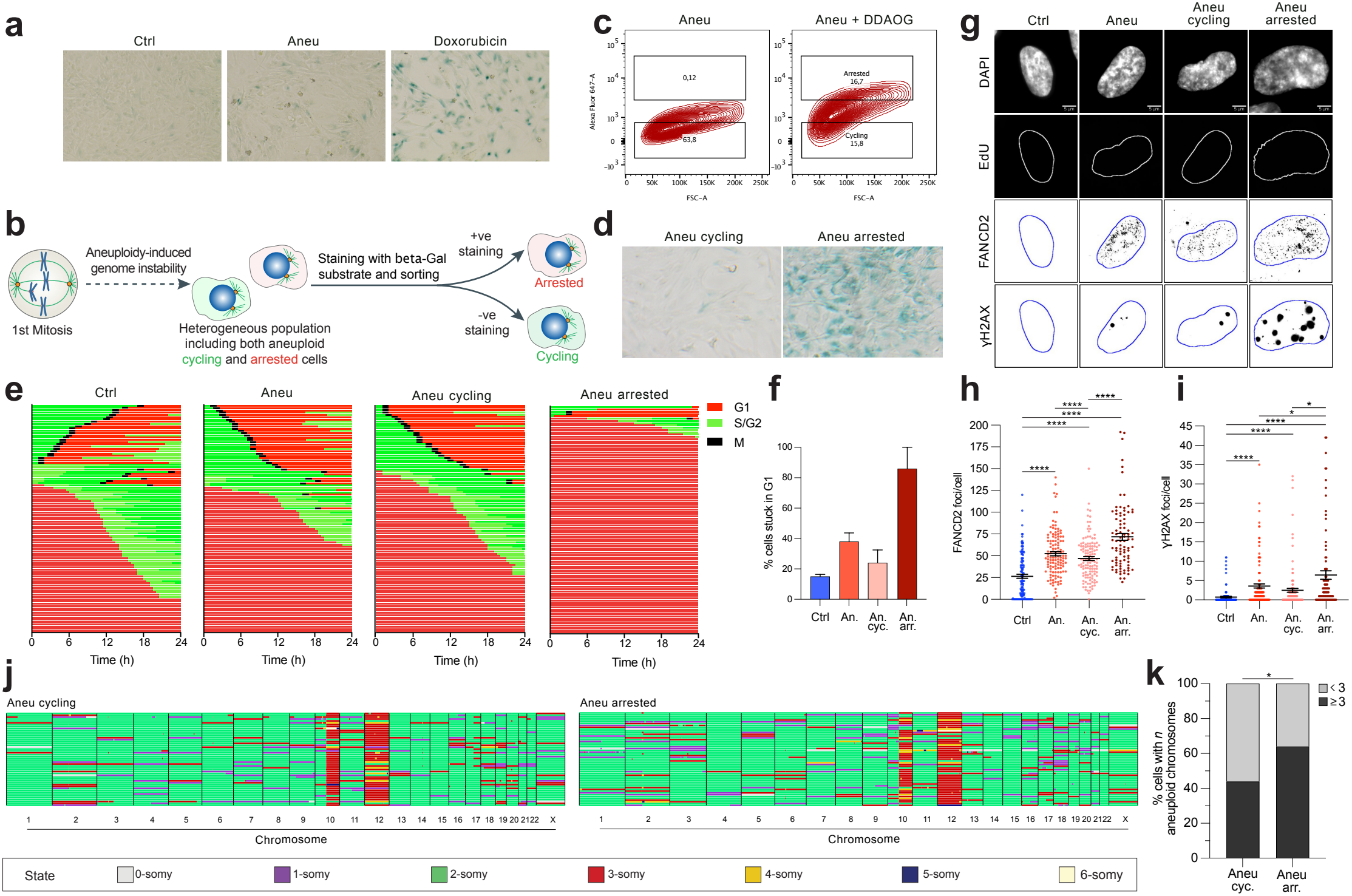
a
Ctrl
Aneu
Doxorubicin
b
Aneuploidy-induced genome instability
1st Mitosis
Heterogeneous population including both aneuploid cycling and arrested cells
Staining with beta-Gal substrate and sorting
+ve staining
-ve staining
Arrested
Cycling
c
Aneu
Aneu + DDAOG
Alexa Fluor 647-A
FSC-A
0,12
63,8
Arrested 16,7
Cycling 15,8
d
Aneu cycling
Aneu arrested
e
Ctrl
Aneu
Aneu cycling
Aneu arrested
G1
S/G2
M
Time (h)
f
% cells stuck in G1
Ctrl
An.
An. cyc.
An. arr.
g
Ctrl
Aneu
Aneu cycling
Aneu arrested
DAPI
EdU
FANCD2
γH2AX
h
FANCD2 foci/cell
i
γH2AX foci/cell
j
Aneu cycling
Aneu arrested
Chromosome
State
0-somy
1-somy
2-somy
3-somy
4-somy
5-somy
6-somy
k
% cells with n aneuploid chromosomes
< 3
≥ 3
Aneu cyc.
Aneu arr.

Figure 5

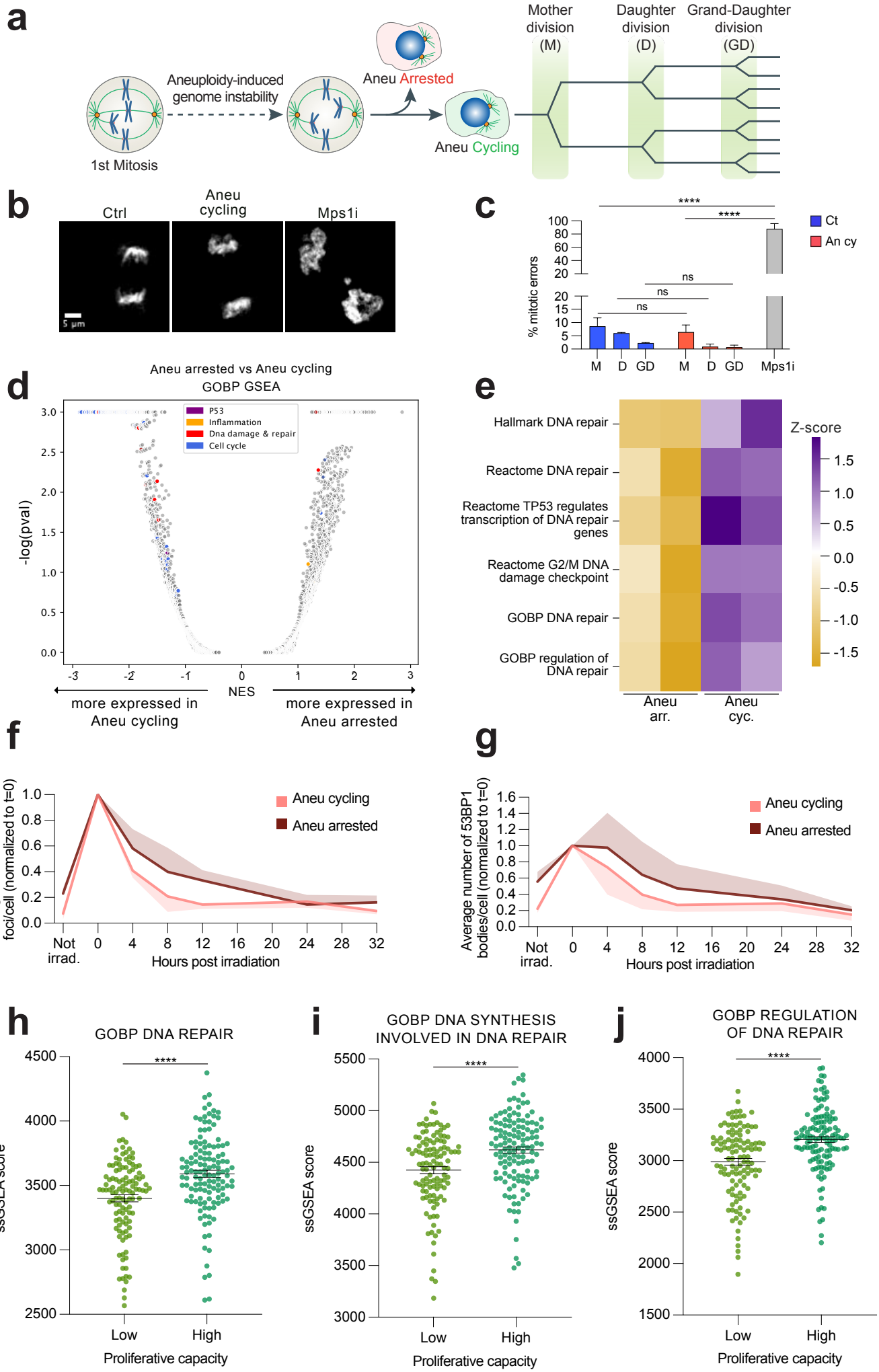

Figure 6

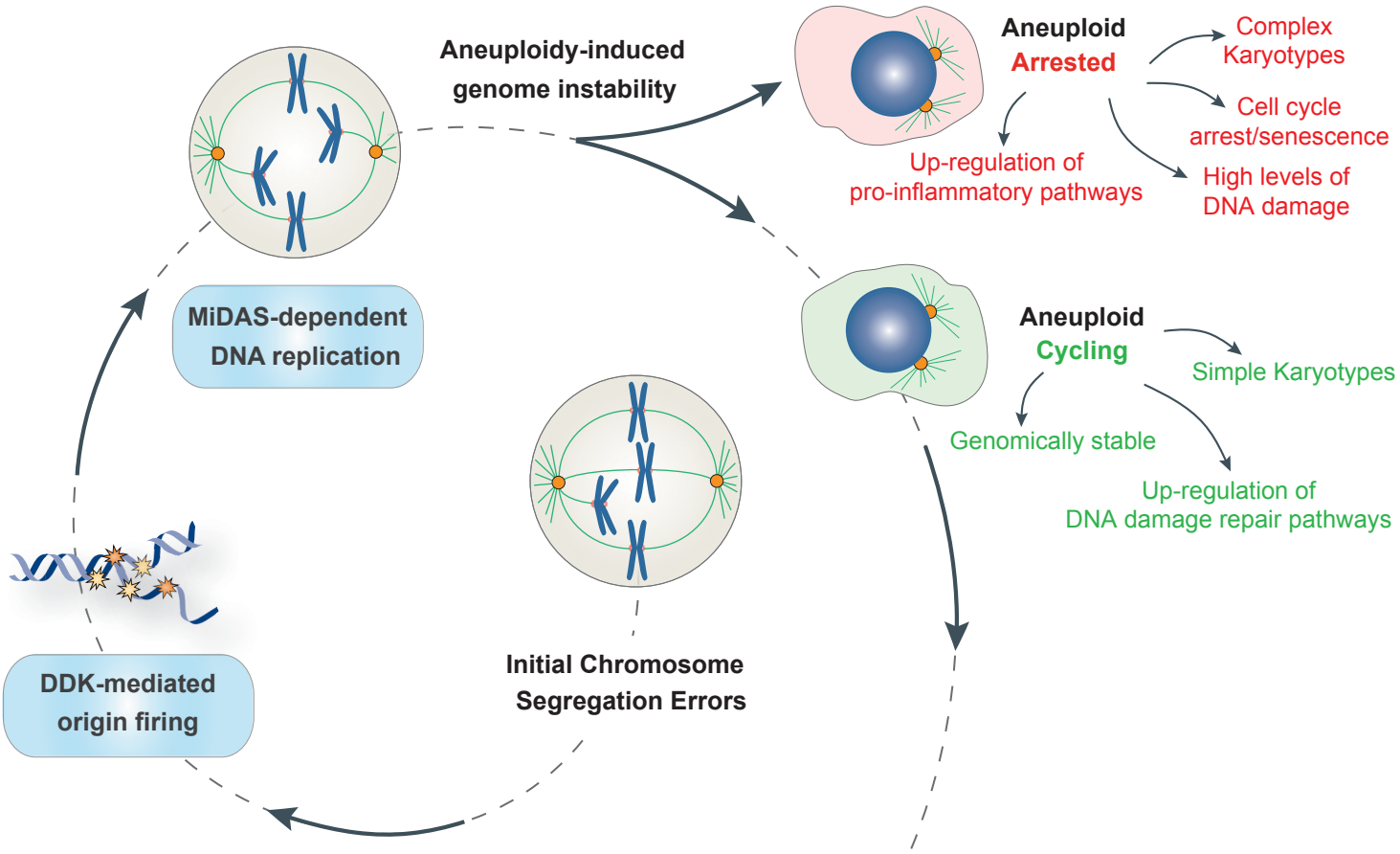

Figure 7

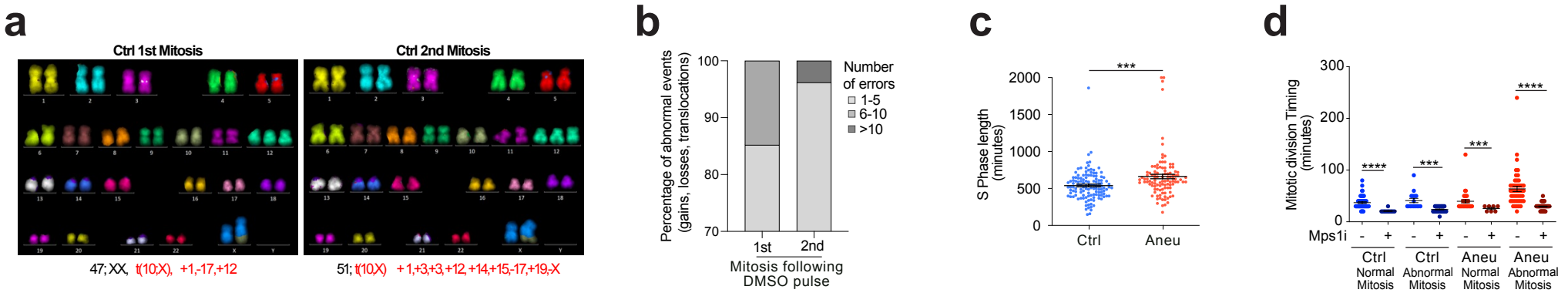

Extended Data Figure 1

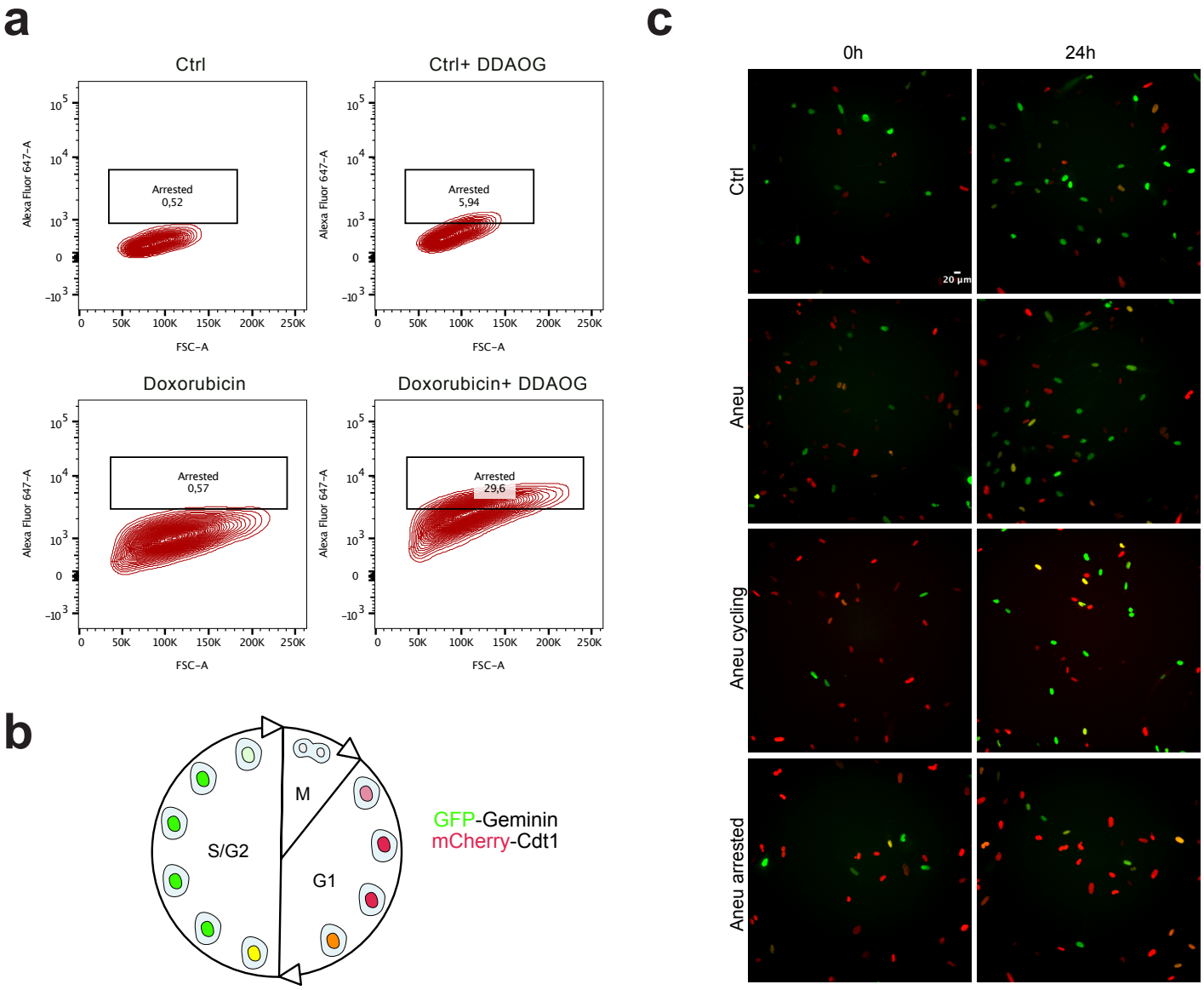

Extended Data Figure 2

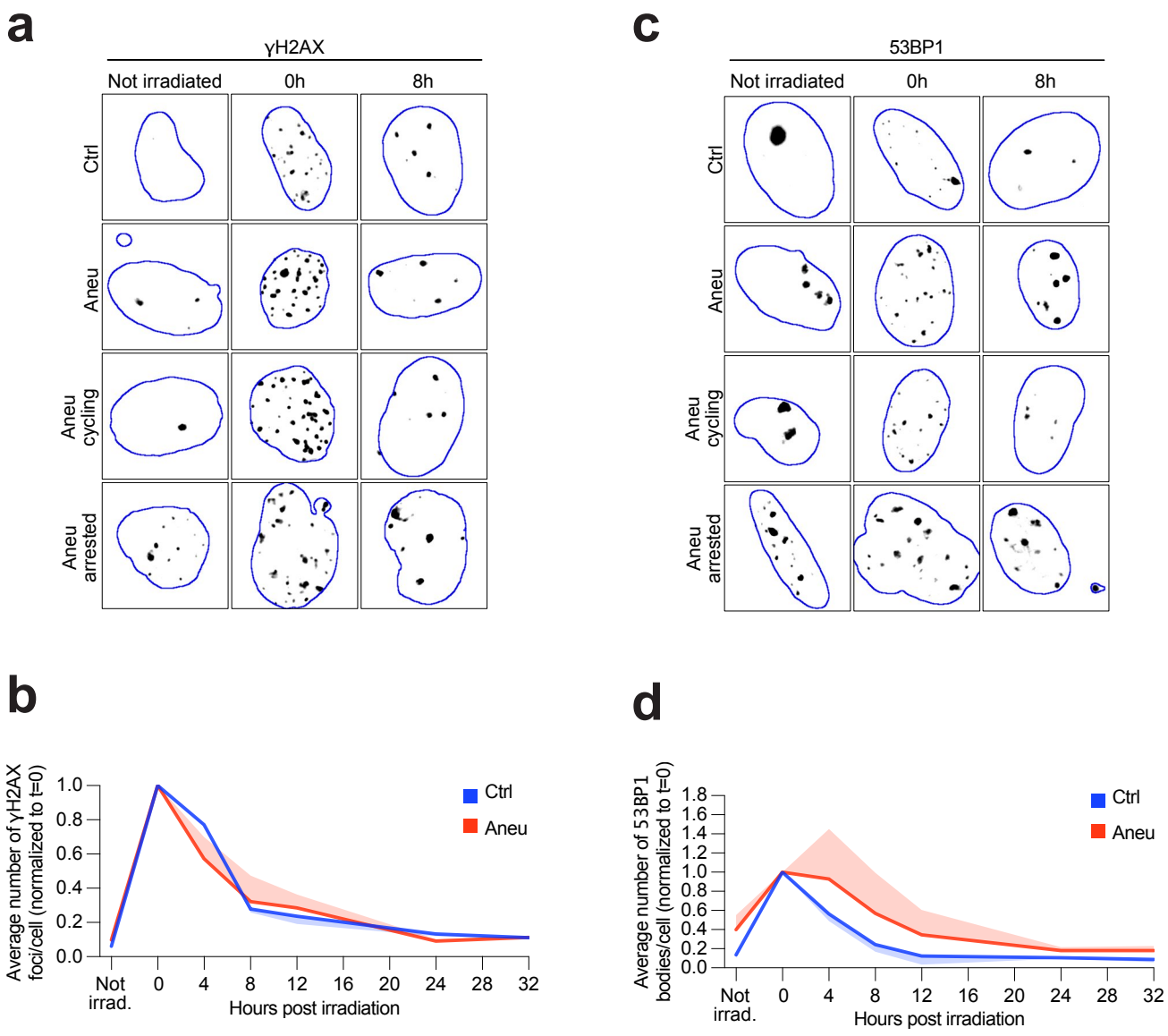

Extended Data Figure 3

gene_name	ensembl_gene_id	baseMean	log2FoldChange	lfcSE	stat	pvalue	padj	signature
UHRF1	ENSG00000276043	992,6407794	-1,463494234	0,23690646	-6,177519319	6,51166E-10	1,46332E-07	GOBP_DNA_REPAIR [569]
FOXM1	ENSG00000111206	1019,397201	-1,365225147	0,581676165	-2,347053616	0,018922532	0,137644121	GOBP_DNA_REPAIR [569]
PRIM1	ENSG00000198056	474,8477874	-1,364119404	0,245844729	-5,548703086	2,87796E-08	3,52553E-06	HALLMARK_DNA_REPAIR [150]
FANCE	ENSG00000112039	267,7712184	-1,343504755	0,283509612	-4,738833176	2,14952E-06	0,000111839	REACTOME_DNA_REPAIR [332]
H2BC14	ENSG00000273703	174,2119743	-1,330320082	0,388364543	-3,425441649	0,000613801	0,010177337	REACTOME_DNA_REPAIR [332]
PTTG1	ENSG00000164611	2092,055002	-1,311532721	0,195952716	-6,693108159	2,1848E-11	9,23032E-09	GOBP_DNA_REPAIR [569]
CCNA2	ENSG00000145386	2017,460861	-1,280223222	0,584722995	-2,189452498	0,028563967	0,180154541	REACTOME_DNA_REPAIR [332]
RAD54L	ENSG00000085999	95,30515172	-1,264984213	0,41289	-3,063731777	0,002185948	0,028823949	KEGG_HOMOLOGOUS_RECOMBINATION [28]
RMI2	ENSG00000175643	198,7630434	-1,256125997	0,317193169	-3,96012941	7,49092E-05	0,002013207	REACTOME_DNA_REPAIR [332]
EME1	ENSG00000154920	125,8010331	-1,251873356	0,378354632	-3,308730094	0,000937201	0,014493003	KEGG_HOMOLOGOUS_RECOMBINATION [28]
HMGB2	ENSG00000164104	2568,528678	-1,247776619	0,623843451	-2,000143812	0,045484737	0,242631208	GOBP_DNA_REPAIR [569]
H4C1	ENSG00000278637	384,8643662	-1,239926814	0,314814741	-3,938591977	8,19612E-05	0,002148074	REACTOME_DNA_REPAIR [332]
BLM	ENSG00000197299	392,269428	-1,238186534	0,264789399	-4,676118227	2,92356E-06	0,000142957	KEGG_HOMOLOGOUS_RECOMBINATION [28]
PIF1	ENSG00000140451	89,12425074	-1,225055521	0,430923506	-2,842860752	0,00447106	0,049708774	GOBP_DNA_REPAIR [569]
H2AX	ENSG00000188486	1633,516624	-1,214070301	0,226237375	-5,366356033	8,03433E-08	7,50961E-06	REACTOME_DNA_REPAIR [332]
MCM2	ENSG00000073111	1471,107745	-1,212075792	0,212945245	-5,691959872	1,25589E-08	1,72269E-06	GOBP_DNA_REPAIR [569]
PCLAF	ENSG00000166803	400,8196156	-1,211648027	0,262104055	-4,622774828	3,78641E-06	0,000178536	REACTOME_DNA_REPAIR [332]
GINS2	ENSG00000131153	692,4481938	-1,198244536	0,216352556	-5,538388641	3,05267E-08	3,62273E-06	GOBP_DNA_REPAIR [569]
CHAF1B	ENSG00000159259	475,6941015	-1,192518656	0,27551539	-4,328319574	1,50251E-05	0,000547535	GOBP_DNA_REPAIR [569]
MCM7	ENSG00000166508	3970,843886	-1,192254667	0,206152086	-5,78337426	7,32169E-09	1,14107E-06	GOBP_DNA_REPAIR [569]
MCM3	ENSG00000112118	2961,430599	-1,179418929	0,179290935	-6,57824071	4,76047E-11	1,7338E-08	GOBP_DNA_REPAIR [569]
POLE2	ENSG00000100479	114,5677156	-1,155770914	0,393054504	-2,940485102	0,003276988	0,039064947	KEGG_BASE_EXCISION_REPAIR [35]
H2BC7	ENSG00000277224	244,6185528	-1,153603703	0,356981821	-3,231547476	0,001231219	0,018061294	REACTOME_DNA_REPAIR [332]
FANCA	ENSG00000187741	276,1320378	-1,147377048	0,323144533	-3,550662107	0,000384263	0,007145405	REACTOME_DNA_REPAIR [332]
ESCO2	ENSG00000171320	604,1535975	-1,131052097	0,254374819	-4,446399614	8,73214E-06	0,000354727	GOBP_DNA_REPAIR [569]
CHAF1A	ENSG00000167670	652,2068713	-1,126431655	0,225719477	-4,990405206	6,02528E-07	3,97744E-05	GOBP_DNA_REPAIR [569]
MCM4	ENSG00000104738	3502,112152	-1,118147714	0,178359277	-6,269075182	3,63199E-10	9,35635E-08	GOBP_DNA_REPAIR [569]
HMGB1	ENSG00000189403	4022,455871	-1,097626305	0,161937686	-6,778078246	1,21785E-11	5,59257E-09	KEGG_BASE_EXCISION_REPAIR [35]
BRCA2	ENSG00000139618	475,1108442	-1,095058696	0,230034854	-4,760403373	1,93206E-06	0,000103063	KEGG_HOMOLOGOUS_RECOMBINATION [28]
DTL	ENSG00000143476	1403,11263	-1,074765995	0,192323372	-5,588327526	2,29267E-08	2,98953E-06	REACTOME_DNA_REPAIR [332]
MCM5	ENSG00000100297	1618,342543	-1,072958858	0,202528225	-5,297823822	1,17191E-07	1,01457E-05	GOBP_DNA_REPAIR [569]
MCM6	ENSG00000076003	1350,168882	-1,070443972	0,191730505	-5,583065521	2,36316E-08	3,04386E-06	GOBP_DNA_REPAIR [569]
XRCC3	ENSG00000126215	153,407276	-1,067855756	0,409861183	-2,605408369	0,009176482	0,083650383	KEGG_HOMOLOGOUS_RECOMBINATION [28]
PAXX	ENSG00000148362	273,4354076	-1,066297861	0,285542718	-3,734284907	0,000188249	0,004057733	GOBP_DNA_REPAIR [569]
ZWINT	ENSG00000122952	1208,569743	-1,057468524	0,216065679	-4,894199437	9,87067E-07	6,06128E-05	HALLMARK_DNA_REPAIR [150]
H2BU1	ENSG00000196890	164,4035717	-1,0526433	0,425867637	-2,471761665	0,013444912	0,107579665	REACTOME_DNA_REPAIR [332]
DDX11	ENSG00000013573	451,5202913	-1,051661549	0,247909922	-4,24211158	2,21427E-05	0,000754422	GOBP_DNA_REPAIR [569]
H2AZ1	ENSG00000164032	7719,34297	-1,050492077	0,167503262	-6,271472355	3,5765E-10	9,35635E-08	REACTOME_DNA_REPAIR [332]
TRIP13	ENSG00000071539	869,8179167	-1,046154634	0,226576705	-4,617220622	3,88914E-06	0,000182389	GOBP_DNA_REPAIR [569]
RAD51	ENSG00000051180	257,3393749	-1,029007726	0,300546848	-3,423784787	0,000617555	0,010223537	HALLMARK_DNA_REPAIR [150]
DNA2	ENSG00000138346	657,8128943	-1,018641876	0,215024678	-4,737325439	2,16557E-06	0,000112121	REACTOME_DNA_REPAIR [332]
UBE2T	ENSG00000077152	667,2240543	-1,00051634	0,248650561	-4,023784771	5,72703E-05	0,001617349	REACTOME_DNA_REPAIR [332]
CLSPN	ENSG00000092853	757,2423379	-0,999979178	0,221806732	-4,508335558	6,53382E-06	0,000289959	REACTOME_DNA_REPAIR [332]
FANCD2	ENSG00000144554	846,2549826	-0,990211718	0,201856287	-4,905528246	9,31762E-07	5,78898E-05	REACTOME_DNA_REPAIR [332]
POLA1	ENSG00000101868	675,0218176	-0,984358017	0,20494672	-4,802994741	1,5631E-06	8,6437E-05	HALLMARK_DNA_REPAIR [150]
MCM8	ENSG00000125885	296,7887492	-0,977502892	0,267888176	-3,648921385	0,000263344	0,005247992	GOBP_DNA_REPAIR [569]
RMI1	ENSG00000178966	149,590574	-0,973469008	0,363808538	-2,675772851	0,007455716	0,072645083	REACTOME_DNA_REPAIR [332]
BRCA1	ENSG00000012048	987,4511882	-0,970000371	0,189075516	-5,130227294	2,89393E-07	2,12261E-05	REACTOME_DNA_REPAIR [332]

Extended Data Table 1